

FTIR ANALYSIS OF HYDROGEN ADSORPTION ON SINGLE WALLED CARBON NANOTUBES

BY STEFFEN KAHLE

A thesis submitted to the
Graduate School—New Brunswick
Rutgers, The State University of New Jersey
in partial fulfillment of the requirements
for the degree of
Master of Science
Graduate Program in Physics
Written under the direction of
Professor Yves J. Chabal
and approved by

New Brunswick, New Jersey

October, 2007

ABSTRACT OF THE THESIS

FTIR Analysis of Hydrogen Adsorption on Single Walled Carbon Nanotubes

by Steffen Kahle

Thesis Director: Professor Yves J. Chabal

The physisorption of hydrogen on Single Walled Carbon Nanotubes (SWNTs) has been spectroscopically studied by Fourier Transform Infrared Spectroscopy at pressures up to 1000 psi and at ambient temperature.

A sample preparation technique has been developed to apply thin films of SWNTs to KBr or Si substrates. The samples showed a broad general absorption which increased with the amount of nanotubes, but it did not show any spectral evidence of the SWNTs or functional groups attached to the nanotubes.

It has been shown, that the broad absorption is due to scattering, which can be reduced by up to 50% by applying a refractive index matching liquid. Furthermore baking up to 700°C increases the transmission by up to 90%, which allows the observation of higher sample amounts.

Measurements at high pressure showed that the hydrogen dipole moment, induced by a perturbation of the electronic distribution of the H₂ molecule due to physisorption

on SWNTs, lies below the sensitivity of the system for samples of up to 2.1 mg of nanotubes.

At the introduction of hydrogen, water as an impurity of the hydrogen has been observed, which adsorbed on the sample surface. Also an increase in the gaseous CO_2 has been detected, which can be caused by adsorped CO_2 on the cell wall which is sputtered off by the impact of the hydrogen molecules at high pressure.

Acknowledgements

This research was done under the supervision of Prof. Yves Chabal and with the help and support of Dr. Jean-Francois Veyan. The sample preparation was made possible by Prof. Manish Chhowalla and Goki Eda. Further thanks goes to Daniel Mayer and Dr. Sylvie Rangan for helpful discussions.

The work was supported by the the U.S. Department of Energy and the German Academic Exchange Service (DAAD).

Dedication

To my parents

Table of Contents

Abstract	ii
Acknowledgements	iv
Dedication	v
List of Figures	ix
1. Motivation	1
1.1. Hydrogen Economy	1
1.2. Hydrogen Storage Systems	2
1.3. Hydrogen Storage in Carbon Nanotubes	5
2. Carbon Nanotubes	7
2.1. Introduction	7
2.2. Synthesis	8
2.3. Purification	9
2.4. Infrared Measurements	11
3. Experimental Techniques	14
3.1. Infrared Spectroscopy	14
3.1.1. Molecular Vibrations	14
3.1.2. Molecular Rotations	17
3.1.3. Polyatomic Molecules	20
3.2. Pressure Induced Spectra	20
3.3. Fourier Transform Infrared Spectroscopy	22
3.3.1. Functional Principle	22
3.3.2. Experimental Considerations	25

4. Experimental Setup	29
4.1. High Pressure Cell	29
4.2. High Pressure	30
4.3. Vacuum	31
4.4. Temperature Control	33
5. Experimental Results	35
5.1. Hydrogen Measurements - Preface	35
5.2. Sample Measurements	35
5.2.1. Samples on KBr Substrate - Preparation	35
Type A	35
Type B	37
5.2.2. Samples on KBr Substrate - Results	38
Comparison of both Sample Types	38
Scattering	40
Peak Assignment	44
5.2.3. Samples on Si Substrate	46
Baking	46
Preparation	47
Results	48
Dropping Method	54
5.3. Hydrogen Measurements	55
5.3.1. Hydrogen Interactions	55
5.3.2. Hydrogen Impurities	60
6. Summary	64
Appendix A. Reference Spectra	66
Appendix B. Cleaning of Silicon	68

References	69
-----------------------------	-----------

List of Figures

1.1. Performance overview of different storage system versus storage targets. Modified from [1]	4
1.2. Illustration of hydrogen storage inside and between of SWNTs. Taken from <i>www.nanotechnologies.qc.ca</i>	6
2.1. Five different allotropes of carbon. Taken from <i>http://en.wikipedia.org/wiki/Carbon</i>	7
2.2. Single walled carbon nanotubes (SNWT), multi walled carbon nanotubes (MWNT)	8
2.3. Schematic presentation of the synthesis and purification process. Modi- fied from [2]	10
2.4. TEM picture of the SWNT's after the purification. Taken from [2]. . . .	11
2.5. Spectra of differently treated SWNT samples. Modified from [3]	13
3.1. Energy levels of an anharmonic oscillator. Taken from [4]	16
3.2. Vibrational spectrum of CO including overtones. Taken from [4]	18
3.3. Term scheme and according spectrum. Modified from [4]	19
3.4. Normal modes of H ₂ O, Taken from [4]	20
3.5. Spectra of pressure induced H ₂ . Taken from [5]	21
3.6. Michelson interferometer. Modified from <i>scienceworld.wolfram.com</i> . . .	23
3.7. Interference of monochromatic light.	24
3.8. Overview of the beam path in the spectrometer. Modified from <i>thermo.com</i>	25
3.9. Examples of spectral data.	27
4.1. Pictures of the high pressure cell and the sample holder. Taken from <i>specac.com</i> and taken by myself.	30
4.2. Schematic of the experiment setup.	31
4.3. Cross section of a turbomolecular pump. Taken from [6]	32

5.1. Photographs of different samples.	37
5.2. Absorbance spectra of KBr-X and KBr-Y.	38
5.3. Absorbance spectra of KBr-50, KBr-100, KBr-200 and KBr-400	39
5.4. Spectra of KBr-X and KBr-400 in direct comparison.	40
5.5. Uncorrected spectra from the samples of method B.	41
5.6. The Intensity of the interferogram for different samples after and before they were treated with Nujol.	41
5.7. Schematic of light scattering with an index-matching liquid.	42
5.8. The intensity of signal ⁻¹ is plotted over the Amount.	43
5.9. Plot of the signal strength over the amount.	43
5.10. Spectra of Si400m after baking to different temperatures.	49
5.11. Spectra of Si400a after baking to different temperatures.	49
5.12. The spectrum of the Si400m sample is compared with the single beam of the plain Si and of an empty chamber.	50
5.13. Spectra of the SiMax1 and SiMax2 sample.	52
5.14. Spectra of the SiDrop sample before and after baking.	55
5.15. Spectra of hydrogen at 700 and 1000 psi.	56
5.16. Hydrogen spectra of KBr100 and of an empty cell both taken at 1000 psi. The subtraction is ten times magnified for better display.	57
5.17. Subtraction spectra for the different samples.	58
5.18. Spectrum showing the time evolution of the adsorbed water.	61
5.19. Plot of the peak area of the adsorbed water over exposure time.	61
5.20. The CO ₂ peak over time. Taken on a KBr sample at 1000 psi.	63
5.21. Time development of the peak area of the CO ₂ peak.	63
A.1. Spectrum of filter paper used in the sample preparation.	66
A.2. Spectrum of SDS (sodium dodecyl sulfate) used in the sample preparation.	66
A.3. Spectrum of a plain KBr pellet	67

Chapter 1

Motivation

1.1 Hydrogen Economy

Mobility of goods and people is a key factor of the modern society. But while most other energy sectors don't depend on a specific source of energy, the transportation sector highly depends on petroleum. While most energy used in domestic or industrial applications is converted to electricity prior to use, the mobile sector demands the storage of the energy carrier on board, which resulted in petroleum being the only choice for over 100 years.

The goal of a possible hydrogen economy is to break this dependence by replacing the petroleum with hydrogen as an energy carrier. This would mean, that energy produced by any primary source can be used to run a car by storing the energy as hydrogen - or to be more precise - to store it as chemical energy in hydrogen. Chemical energy is the potential of unpaired valence electrons to pair with electrons from other atoms. Because hydrogen offers the best possible ratio of unpaired electrons per mass, it is a highly attractive energy carrier [7].

Hydrogen is the most abundant element on earth, but almost all of it is bound in compounds like water or hydrocarbons. Molecular hydrogen gas can not be found in nature, so it has to be produced from its compounds. While the extraction from water by electrolysis or thermal dissociation is chemically clean, it costs vast amounts of energy. Obtaining hydrogen from hydrocarbons is more energy efficient but does not solve the main problem. So the ecological impact of hydrogen as an energy carrier depends on the method hydrogen is produced.

Once obtained hydrogen is a clean synthetic fuel. The stored energy can be retracted by burning it with oxygen producing only water as an exhaust gas. There exist two different ways to run a car on hydrogen. It can be burned in a conventional combustion engine with efficiencies up to 25%, which is slightly better than the values for conventional systems [7], or it can be recombined with oxygen electrochemically in a fuel cell to produce electricity. Because the latter process is not a heat engine, it is not limited by the carnot process. Modern PEMFC (proton exchange membrane fuel cells) reach efficiencies up to 60% [7]. While a fuel cell produces electrical energy, which still has to be converted to mechanical energy to run the car, a combustion engine produces mechanical energy directly. Even though the tank-to-wheel efficiency of a fuel cell system can reach 40% compared to 22% for a diesel engine assuming a realistic driving behaviour [8].

1.2 Hydrogen Storage Systems

A major problem today is the storage of hydrogen. While hydrogen has three times the gravimetric energy density compared to gasoline (120 MJ/kg for hydrogen versus 44 MJ/kg for gasoline [9]), the volumetric energy density is much lower for hydrogen than for gasoline. Because hydrogen is a gas at ambient conditions, the volumetric density depends on the pressure. The natural limit of contraction is the density of liquid hydrogen, where the volumetric density is one fourth of the one of gasoline (8 MJ/l for liquid hydrogen versus 32 MJ/l for gasoline) [9]. The low volumetric density is the key problem to be solved in H storage.

To face this challenges the U.S. Department of Energy (DOE) has started the National Hydrogen Storage Project, which also provided funding for this project. The DOE has stated several performance targets on storage systems, which are necessary to compete with todays gasoline vehicles [9]. Some of the major requirements can be

seen in table 1.1. Additionally to those requirements given in the table the system has to operate at ambient temperature and fulfill certain durability, safety and cost requirements. The claimed energy densities always incorporate the weight or size of the whole system. This includes the tank, valves, piping, insulation, cooling devices, etc.

Storage parameter	Units	2010	2015
Gravimetric density	kWh/kg (kg H ₂ /kg system)	2 (0.06)	3 (0.09)
Volumetric density	kWh/l (kg H ₂ /l system)	1.5 (0.045)	2.7 (0.081)
System Fill time (for 5 kg)	min	3	2.5

Table 1.1: Some of the U.S DOE hydrogen storage system performance targets for the years 2010 and 2015, [9]

There have been several approaches to fulfill those requirements, even though no system has fulfilled all requirements yet. Because with classical approaches like high pressure or liquefied hydrogen no breakthrough seems to be achievable, other options like metal hydrides or adsorption at high surface carbon materials are being explored. Those technologies try to bind the hydrogen either by chemisorption or by physisorption to another material. Figure 1.1 gives an performance overview of the different technologies. In that figure the gravimetric capacity is expressed in weight percent (wt%), which is the percentage of stored hydrogen divided by the weight of the complete system and the hydrogen.

High pressure hydrogen tanks are built from carbon fibers materials to obtain a better weight performance than with steel tanks. The automobile industry has implemented that technique in prototypes with tanks up to 700 bar. As can be seen in fig. 1.1 those pressures are far from meeting the DOE standards in volumetric capacity. The necessary compression energy (up to 20% of the lower heating value) reduces the overall efficiency and the typical cylindrical shapes of the tanks causes problems in placing it in the vehicle. While higher pressure can improve the volumetric capacity, the implied reinforcements in the tank structure seem to discourage from use of higher pressures,

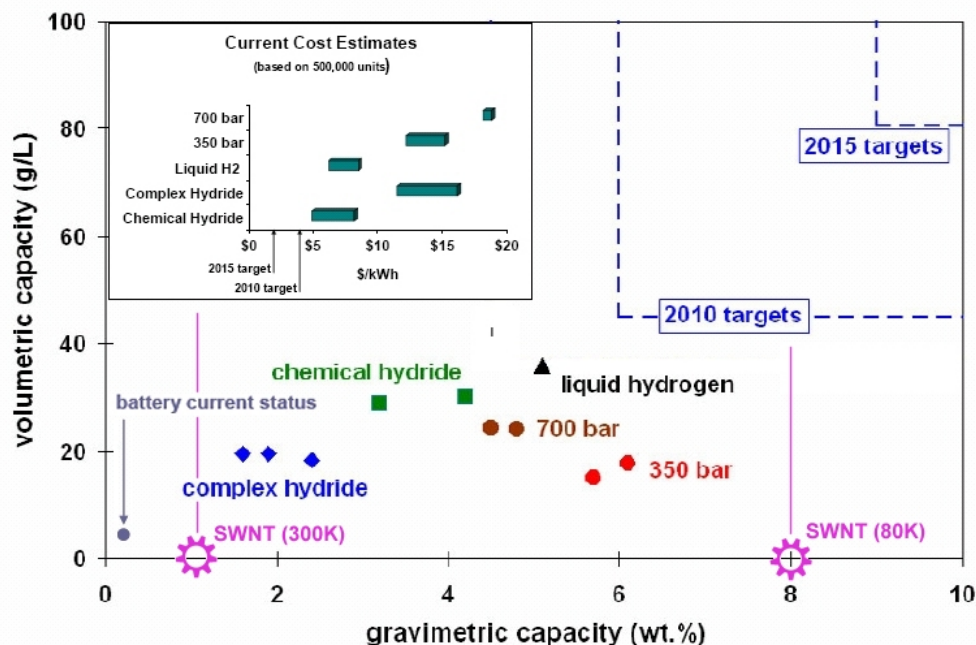


Figure 1.1: Performance overview of different storage system versus storage targets. The gravimetric capacity of single walled carbon nanotubes (SWNT) at different temperatures has been added. No volumetric capacity has been available. This publication splits metal hydrides in two subtypes according to the quantity of different elements. (chemical = H-X, complex = H-X-Y)

so that no major improvements are expected from this technology.

Cryogenic liquefied hydrogen offers high volumetric capacity at temperatures below the boiling point of hydrogen at 21 K. The liquefaction energy is over 30% of the lower heating value, which is the major drawback of this technology. The second key issue is hydrogen boil-off due to warming up off the liquid. Hydrogen boil-off happens also when the car is parked and can be 1% per day or more [9]. If the car is parked in a confined space like a garage, boiled-off hydrogen is also a safety issue. While the boil-off can be minimized by better (and more heavy) insulation, the loss of liquefaction energy is an intrinsic problem.

A hydride is the negative hydrogen ion H^- , which can form crystal structures with other materials. Materials investigated for hydrogen storage are metal hydrides of Li,

Na or Al. To use crystal structures as a reversible storage device, it is a key requirement to be able to release the hydrogen near room temperature and at low pressure. While release at high values not only consumes energy, fuel cells also need to be fed with hydrogen at certain conditions (25-120°C, 1-10 atm [9]). Furthermore the refueling process of metal hydrides is problematic due to slow reaction kinetics and high enthalpies caused by strong chemical bonds. The use of catalysts is being investigated to reduce the decomposition energy and increase the kinetics.

High surface area carbon materials can physisorb hydrogen and therefore offer lower binding energies, which potentially fewer thermal problems than in metal hydrides. Materials of interest are e.g. carbon nanotubes, graphene sheets and metal organic frameworks (MOF). An advantage of carbon materials is their variable structure, which allows the material to be specifically modified to optimize it for hydrogen uptake. An uptake of 7.5 wt% at cryogenic temperatures and of 0.4 wt% at room temperature has been found for MOFs [10].

1.3 Hydrogen Storage in Carbon Nanotubes

Hydrogen uptake in carbon nanotubes has first been observed by Dillon [11] in 1997 who claimed 10 wt% of hydrogen storage¹. This promising result led to a high research activity in the following years, where uptake values between 1 wt% and 10 wt% have been reported for different carbon structures including single walled carbon nanotubes (SWNTs) [12, 13]. Many of those results could not be reproduced or have shown to be erroneous. Common problems have been that leaks in the system have been perceived as hydrogen storage [14] or other experimental difficulties. Because all known nanotube syntheses produces a lot of by-products, nanotubes are usually purified before hydrogen storage. The contaminants in the samples lead to a poor sample reproducibility [15] and the hydrogen storage is highly dependant on the sample preparation [16].

¹Dillon's results have been corrected later to lower values.

Recently more critical experiments and reviews of the old publications have shown lower uptake values. At room temperature Zacharia [17] reported 0.15 wt% at 230 psi while Tibbets [14] just set an upper limit of 0.5 wt% at 500 psi. Ye [13] reported 8 wt% at 80K. While the uptake is still a controversial topic, it can be agreed that SWNT do not store more than 1 wt% per 1500 psi at room temperature [18, 14].

The mechanism of hydrogen storage on SWNT at room temperature or below is believed to be physisorption [19, 20], while chemisorption has been reported at high temperatures and pressures of 1500 psi [21]. While on a flat carbon surface the weak van der Waals force of the physisorption could only store one monolayer, the potential inside the nanotubes reaches lower energies to allow higher storage amounts. The ideal tube diameter equals a few molecular diameters of hydrogen and has been calculated for storage at room temperature to be 1.2 nm [22]. Because SWNTs tend to form bundles of individual tubes further storage of hydrogen is expected to occur between the individual tubes.

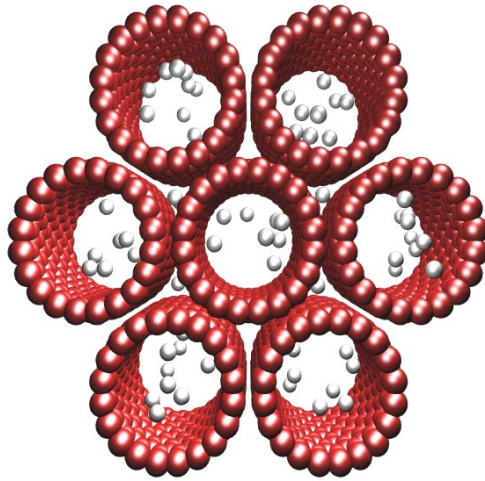


Figure 1.2: Illustration of hydrogen storage inside and between of SWNTs.

To allow access to the inside of the tubes, the endcaps have to be removed, which can be chemically controlled. Doping with alkali-metals has been shown to enhance the storage capabilities to up to 2.5 wt% at ambient conditions [15, 22].

Chapter 2

Carbon Nanotubes

2.1 Introduction

Carbon is the basis for the chemistry of all known life. The reason for that is the flexibility of the four valence electrons, which can hybridize in sp , sp^2 or sp^3 configuration. This allows carbon to appear in many different allotropes. The three natural allotropes of carbon are diamond, graphite and amorphous carbon, which can be seen in figure 2.1. The diversity of artificially formed allotropes is much bigger and figure 2.1 shows fullerenes and nanotubes as two of them.

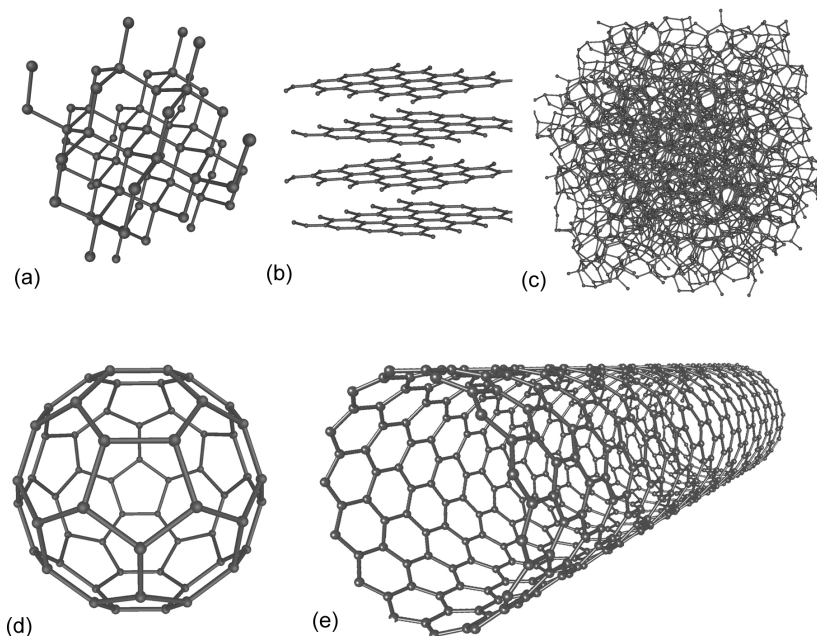


Figure 2.1: Five different allotropes of carbon. (a) diamond, (b) graphite, (c) amorphous carbon, (d) C₆₀ fullerene, (e) single walled carbon nanotube

Since their discovery by Iijima in 1991 [23] carbon nanotubes have been widely investigated in their mechanical, electrical, thermal and chemical properties. Two kinds of nanotubes can be distinguished.

Single walled carbon nanotubes (SWNT) consist of a seamlessly rolled up graphene sheet forming a cylinder which can be capped by a fullerene-like hemisphere or which can be open. Different rolling directions (chirality) are leading to either metallic or semiconducting materials. The diameter of SWNT can range from 0.4 nm to 5 nm and their lengths is usually several micrometers [2]. SWNTs are likely to form bundles of up to hundreds of individual tubes, which can be seen in figure 2.4

Multi walled carbon nanotubes (MWNT) consist of several concentric cylinders as shown in figure 2.2. The distance between the layers is similar to the distance of the layers in graphite (0.34 nm) and a MWNT can consist of up to 50 shells.

In this work SWNT's are used due to their higher hydrogen uptake values

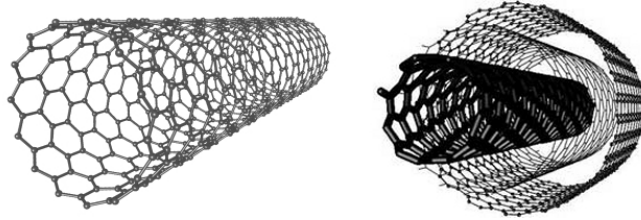


Figure 2.2: Single walled carbon nanotubes (SNWT), multi walled carbon nanotubes (MWNT)

2.2 Synthesis

The carbon nanotubes used in this experiment are provided by the research group of M. Chhowalla from the Material Science department at Rutgers, whose equipment was used for the sample preparation performed in this work. The material is synthesized by the high pressure carbon monoxide (HiPCO) method as it is described in [2] or [24].

This method exploits the decomposition of carbon monoxide to form carbon nanotubes.



The reaction occurs catalytically on the surface of iron nanoparticles, as schematically shown in figure 2.3. This catalyst is provided by the precursor $\text{Fe}(\text{CO})_5$, which decomposes at high temperatures to iron nanoclusters. The process is performed under high CO pressure to improve the yield.

The so produced SWNTs have a diameter of about 1.2 nm and a length of 1-3 μm . It has to be noticed, that a synthesis process for carbon nanotubes always produces a certain distribution of tube diameters and lengths instead of exactly identical tubes - so given numbers are always average values. The chirality of the tubes has not been studied, but it has been discovered that 1/3 of them are metallic and 2/3 are semi-conducting.

2.3 Purification

The synthesis produces nanotubes of a purity of $\sim 80\%$ [2], which is contaminated from byproducts of the synthesis like iron particles and amorphous or graphitic carbon, which encapsulate the iron. To remove these byproducts a usual approach is a two step process, which includes first a strong oxidation followed by an acid reflux.

As a first step the material is annealed in dry air for 24h at 225°C . This leads to oxidization of the amorphous carbon to carbon dioxide and of the iron to iron oxide. The oxidation of the iron induces a volume change, which cracks up the encapsulation of the iron particle.

As a second step the material is stirred in 6M hydrochloric acid (HCl) for 24h followed by sonication for 20min in 6M HCl and for 2h in 12M HCl both at 80°C . This treatment removes the metallic catalyst by at least two orders of magnitude [2].

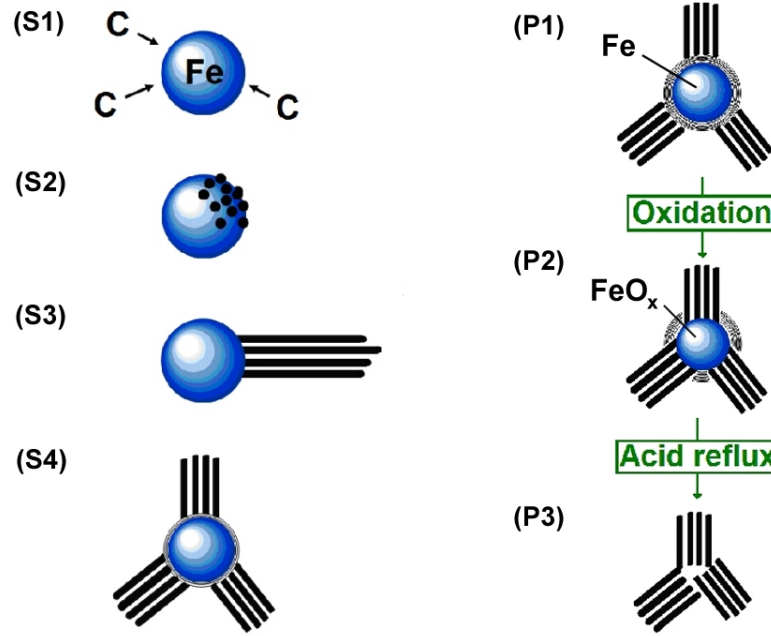


Figure 2.3: Schematic presentation of the synthesis (left) and purification (right) process. (S1) Iron particle interacting with surrounding carbon, (S2) Nucleation of SWNT, (S3) Growing of SWNT, (S4) & (P1) Iron catalyst encapsulated by amorphous and graphitic carbon, (P2) Carbon encapsulation breaks open when iron is oxidized, (P3) Purified SWNT

Because the oxidation of the first step causes damage of the SWNT structure, the material is annealed to 1000°C for 1h under argon atmosphere after the purification process, which leads to a reconstruction of the structure.

As mentioned in section 1.3 the endcaps of the nanotubes have to be removed to allow hydrogen molecules to adsorb inside the nanotubes. The tubes are opened by breaking the highly strained bonds holding the endcaps, which is done by the sonication with HCl. The yield of this process can be improved by exposure to concentrated nitric acid [25]. In the acid environment the open bonds are usually occupied by carboxylic groups ($-\text{COOH}$).

For further sample preparation the nanotubes are put in dispersion to allow easy handling. Because nanotubes have the tendency to form bundles or ropes consisting

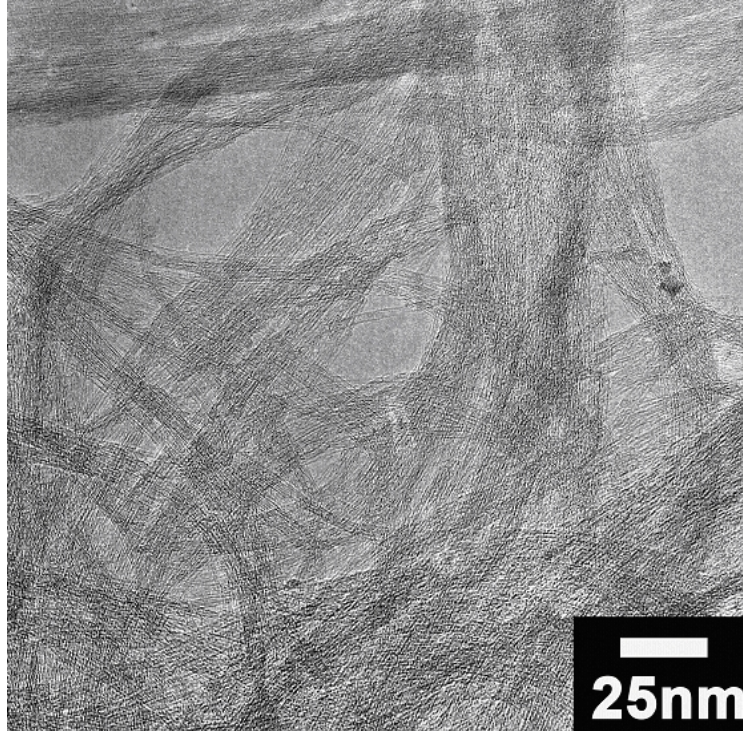


Figure 2.4: TEM picture of the SWNT's after the purification.

of several individual tubes, they can not form a stable solution in water. Therefore they are dispersed in water with 1wt% SDS (sodium dodecyl sulfate) as a surfactant molecule while sonicating, which forms a relatively stable dispersion. The SDS adsorbs on the NT walls and prevents the agglomeration to bundles.

Solutions of up to a few mg/l are stable for storage. At higher concentrations the nanotubes are reforming bundles, which can be dispersed again by intensive sonication.

2.4 Infrared Measurements

Ideally SWNTs consist only of C-C bondings, which have no intrinsic dipole moment. Therefore the IR signal is generated by dynamic dipole moments which are in general much weaker than permanent ones and thus hard to observe [3].

Therefore IR studies on SWNTs are usually used to identify functional groups like

carboxyl- (-COOH) or hydroxyl- (-OH) groups, which have a much bigger IR cross section than the nanotubes itself. E.g. Kuznetsova [26] reported carboxyl groups attached to carbon nanotubes at 3644 cm^{-1} , using a treatment of H_2SO_4 and HNO_3 to prepare the samples.

Infrared active modes of nanotubes have been calculated by Dresselhaus [27] and have been observed recently by Kim [3, 28]. According to Dresselhaus modes with energies of more than 400 cm^{-1} show only weak dependence of the tube diameter, which makes measurements on different samples comparable.

According to [3] and [28] the optical density in the IR range is dominated by an electronic transition, which produces a curved baseline with a minimum around 1600 cm^{-1} . A spectrum is shown in figure 2.5.

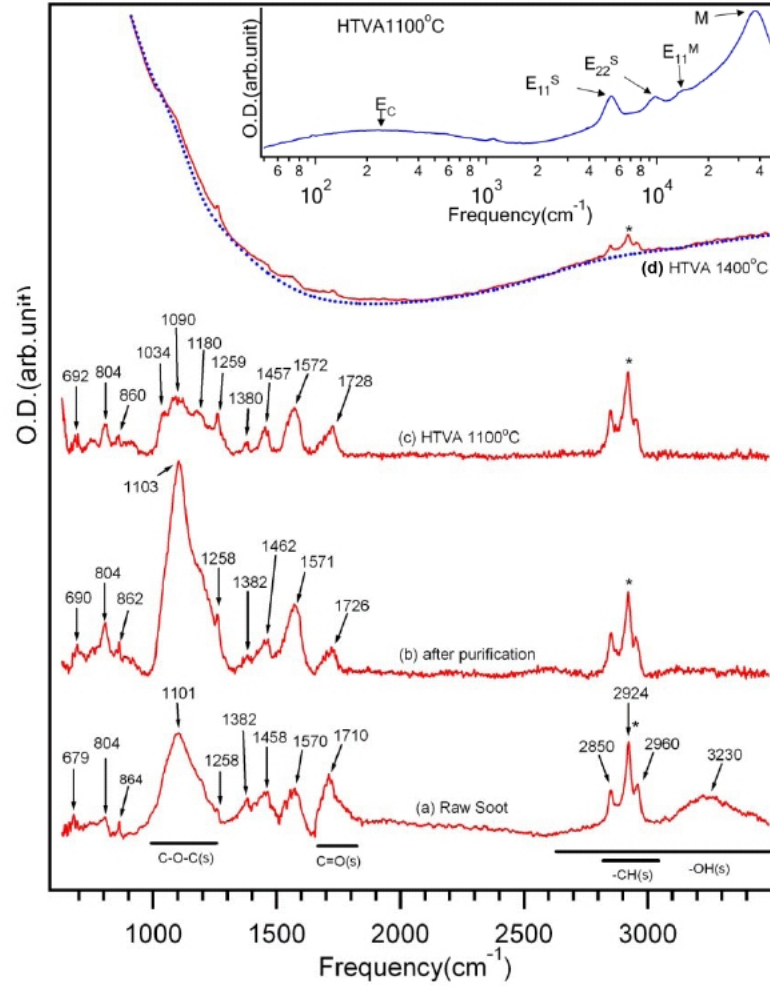


Figure 2.5: Difference Spectra of SWNT samples in transmission. (a) raw soot, (b) after purification, (c) after purification and vacuum annealing at 1100 °C, (d) after purification and vacuum annealing to 1400 °C and a polynomial fit for a flat background. The inset shows the entire spectrum after 1100 °C. The asterisk indicates a hydrocarbon contamination of the spectrometer and does not belong to the SWNT signal. Taken from [3]

Chapter 3

Experimental Techniques

3.1 Infrared Spectroscopy

Infrared spectroscopy is an experimental technique which exploits the fact that only certain rotational and vibrational energy values are allowed for a molecule. It is easy to use and gives quickly results which makes it a popular analyzing technique today. Most commonly it is used in a transmission setup measuring the absorption properties of the sample, like it is done in this work also.

3.1.1 Molecular Vibrations

A quantum mechanical system like a molecule is confined to be in a certain state with an according eigenenergy. If this system is exposed to a periodic perturbation H_1 we can compute the transition probability from one state i to another state f using Fermi's Golden Rule [29] to be

$$R_{i \rightarrow f} = \frac{2\pi}{\hbar} |\langle f | H_1 | i \rangle|^2 \delta(E_f - E_i - \hbar\omega) \quad (3.1)$$

If we use a light wave as the periodic perturbation we can describe that perturbation by the dipole operator \vec{p} . We see that transitions are only possible if the matrix element is non-vanishing. We can analyze the matrix element by splitting up the dipole operator in the electronic part and the nuclear part. We also factorize the wave function accordingly and get

$$\langle f | \vec{p} | i \rangle = \langle f_e f_n | \vec{p}_e + \vec{p}_n | i_e i_n \rangle \quad (3.2)$$

As seen in Fermi's Golden Rule (eq. 3.1) a transition can only take place if the perturbing light wave has the correct amount of energy, which equals the difference

between the two energy levels. Because the energy necessary to excite an electronic transition is higher than the energy provided by a photon in the IR range [4], we know that the electronic state does not change ($i_e = f_e$). Therefore the electronic term vanishes, because the dipole operator is odd

$$\langle f_e f_n | \vec{p}_e | i_e i_n \rangle = \langle i_e | \vec{p}_e | i_e \rangle \langle f_n | i_n \rangle = \vec{0} \quad (3.3)$$

The matrix element is now reduced to the nuclear part which describes rotational and vibrational excitations.

$$\langle f | \vec{p} | i \rangle = \langle f_n | \vec{p}_n | i_n \rangle \quad (3.4)$$

It can be seen that a homonuclear molecule, having no dipole moment, would have a vanishing matrix element. In more applied terms this means, that the light wave needs a dipole moment to interact with.

Now we think about the energy values our system can take. For simplicity we assume a diatomic molecule. The intramolecular bond can be described in first approximation by a harmonic potential

$$V = k (R - R_e)^2 \quad (3.5)$$

where R is distance between both atoms and R_e the equilibrium distance with the lowest energy. The eigenenergies of this system are given by

$$E = \hbar \omega_e \left(\nu + \frac{1}{2} \right) \quad \nu = 0, 1, 2, \dots \quad (3.6)$$

with the eigenfrequency ω_e of the molecule.

The energy difference between two energy levels is $\hbar \omega_e$ which is usually much higher than the thermic energy at room temperature. Thus in thermal equilibrium almost only the ground state is occupied. Because of this spectroscopic techniques cannot observe emissions on those systems, but have to measure absorption by providing photons with the appropriate frequencies.

If we compute the matrix elements for this system we derive the selection rule that only transitions with $\Delta\nu = \pm 1$ are allowed[4]. Therefore only one single peak at $\hbar\omega_e$ would be seen in an absorption spectra.

For a more accurate modeling of the intramolecular potential the Morse potential is often used (fig. 3.1).

$$V = D_e \left[1 - e^{-a(R-R_e)} \right]^2 \quad (3.7)$$

Here D_e is the dissociation energy and the constant a is given by $a = \sqrt{m/2D_e} \omega_e$, with the reduced mass m and the eigenfrequency ω_e .

For R around R_e the Morse potential can be approximated by a harmonic oscillator. Improvements of the Morse potential compared to the harmonic oscillator are the finite dissociation energy and the asymmetric behavior at higher energies which can explain the phenomena of thermal expansion.

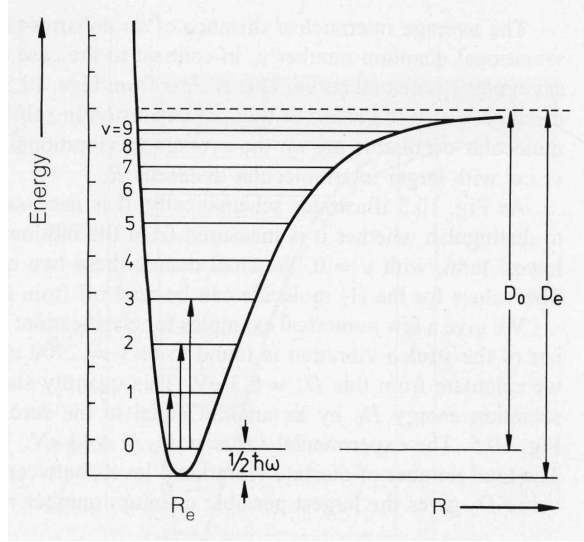


Figure 3.1: The energy levels of an anharmonic oscillator

The eigenenergies of the Morse potential are described by the following series expansion

$$E = \hbar\omega_e \left[\left(\nu + \frac{1}{2} \right) - \chi_e \left(\nu + \frac{1}{2} \right)^2 + \dots \right], \quad \nu = 0, 1, 2, \dots \quad (3.8)$$

χ_e is the anharmonicity constant which is given by $\chi_e = \frac{\hbar\omega}{4D_e}$ and is usually small compared to one. Terms higher than second order can usually be neglected. As expected the energies for low ν are similar to those of the harmonic oscillator. According to the uncertainty principle we see that the system holds a zero-point energy so two different definitions of dissociation energy arise as can be seen in figure 3.1.

The selection rule $\Delta\nu = \pm 1$ from the harmonic oscillator is not strictly valid anymore. The new selection rule is

$$\Delta\nu = \pm 1, \pm 2, \pm 3, \dots \quad (3.9)$$

The higher transitions, also called *overtones*, are much less probable than the basic transition.

The energy differences are now different for each pair of energy levels. As mentioned above excitations from the ground state are the most common transitions and occur at the energies

$$\Delta E_{1 \leftarrow 0} = \hbar\omega_e (1 - 2\chi) \quad (3.10)$$

$$\Delta E_{2 \leftarrow 0} = 2\hbar\omega_e (1 - 3\chi) \quad (3.11)$$

$$\Delta E_{\nu \leftarrow 0} = \nu \hbar\omega_e (1 - \chi(\nu + 1)) \quad (3.12)$$

So in addition to our main excitation $\Delta E_{1 \leftarrow 0}$ we see the overtone peaks at energies close to multiples of the main peak and with much less intensity. An example of that can be seen in figure 3.2

3.1.2 Molecular Rotations

A molecule can not only vibrate but also rotate. In the quantum mechanical description it can assume several rotational states J , therefore also rotational transitions are possible. Assuming a molecule with a non-vanishing dipole moment, it is obvious that this dipole moment changes while rotating, so rotational transitions can be excited by

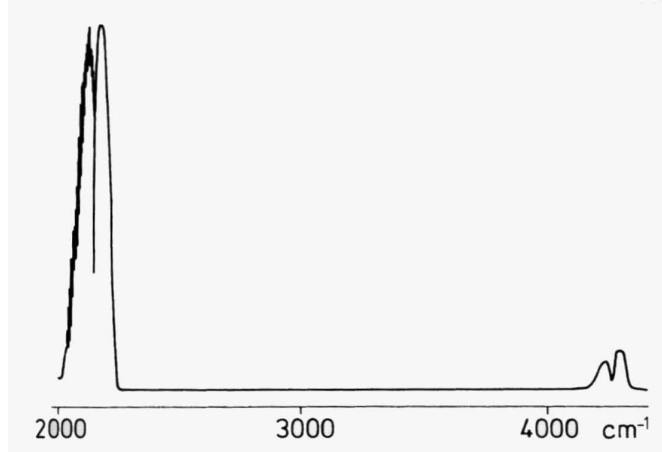


Figure 3.2: The vibrational spectrum of CO. We see the main excitation at 2143 cm^{-1} and the first overtone at 4260 cm^{-1} . Note that the overtone has less intensity than the main excitation.

light waves and thus are observable by spectroscopic observations.

The rotational transitions are much lower in energy than vibrational transitions and can be found in the microwave spectra. They are anyway of interest for IR spectroscopy, because rotational and vibrational transitions happen at the same time. In the IR range we observe therefore these combined excitations instead of pure vibrational spectra. Around the vibrational frequency we can see several individual peaks which form so called *bands*.

The selection rule for rotational transitions is $\Delta J = \pm 1$ and the energy levels behave according to $E_J \propto J(J+1)$ [4]. So the energy difference between two adjacent levels increases with the quantum number J , leading to a separate peak for each transition.

Contrary to the vibrational spectra more than just the ground level is occupied, because the energy differences are small compared to $k_B T$ at room temperature. So several peaks are observed in a rotational spectra.

In figure 3.3 we see an example of a rotational vibrational spectrum. The transitions are taking place from $(J'', \nu'' = 0)$ to $(J', \nu' = 1)$. We can see the different excitation

energies according to initial state J'' .

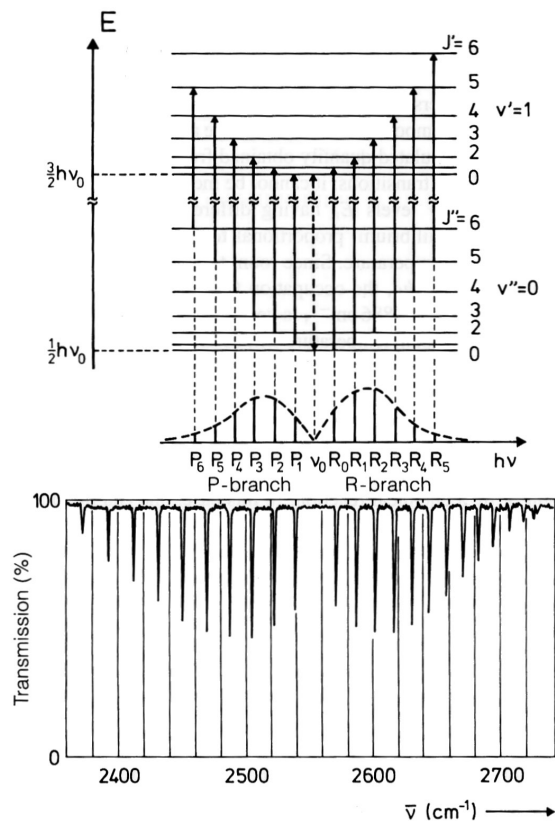


Figure 3.3: Bandspectrum of HBr, showing the term scheme and the according transmission spectrum. The occurrence of individual peaks reasoned to the energy scheme is shown.

The peaks with higher energy than the basic transition at ν_0 form the so called R-branch, those with lower energy the P-branch. Transitions of the R-branch increase the quantum number J by one and those of the P-branch decrease it by one.

As we can see in figure 3.3 there is no pure vibrational transition ($\Delta J=0$) allowed. A classical explanation here is, that a change in the vibrational state is also a change in the bond length. So a change of the bond length will influence the rotational energy of the system. Only when a molecule is rotating around the axis, in which the vibration takes place, a transition with $\Delta J = 0$, the Q-branch, is allowed.

The structure seen in figure 3.2 appears to be a double peak representing the two

bands of the CO_2 molecule. Due to insufficient resolution the finer details of the bands are not visible anymore, which is also the case for most measurements taken in this work.

3.1.3 Polyatomic Molecules

While diatomic molecules have only one vibrational mode, we have to take into account that polyatomic molecules have several vibrational modes. In addition to stretching modes parallel to bonding axis they have bending modes (cf. fig. 3.4). All possible vibrations can be described as a superposition of normal modes. The number of normal modes can be derived by the consideration, that each system of N particles has $3N$ degrees of freedom. We consider three of that degrees to the translational and three to the rotational movement of the molecule. So there are $3N - 6$ degrees remaining, which is the number of normal modes. Note that in the case of a linear molecule there is no rotation around the molecule axis and so the number of normal modes is $3N - 5$.

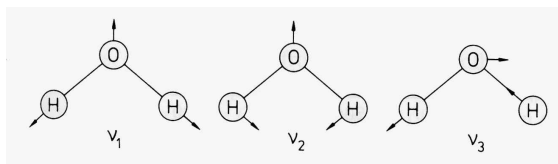


Figure 3.4: The three normal modes of a H_2O molecule. ν_1 is a stretching mode and ν_2 and ν_3 are bending modes.

So for each molecule we can observe several modes in our spectra. This is especially important for condensed phases.

3.2 Pressure Induced Spectra

It was mentioned above that molecule needs a dipole moment to interact with the electromagnetic field of a light wave and so to be detectable with infrared spectroscopy. A hydrogen molecule is a homonuclear diatomic molecule and therefore has no dipole moment and thus cannot be detected. But so far our considerations have been based only on isolated molecules; at high density the interaction of the hydrogen molecules with each other has to be taken into account.

While the electronic distribution of a single H_2 molecule is symmetric, it can be disturbed in a collision event of two or more molecules and so a temporary dipole moment can be established. This dipole moment is modulated by the rotational and vibrational states of the collision partners and also of the movements of the collision partners.

The pressure induced absorption is due to two different effects. The quadrupolar moment (which by itself is not detectable) of one molecule induces a dipole moment in another molecule or these induction is due to the overlap of the electronic clouds. While the first process has a selection rule of $\Delta J = 0, \pm 2$, the latter one produces mainly transitions with $\Delta J = 0$ [30]. Accordingly we observe Q- and S-branches in our spectra.

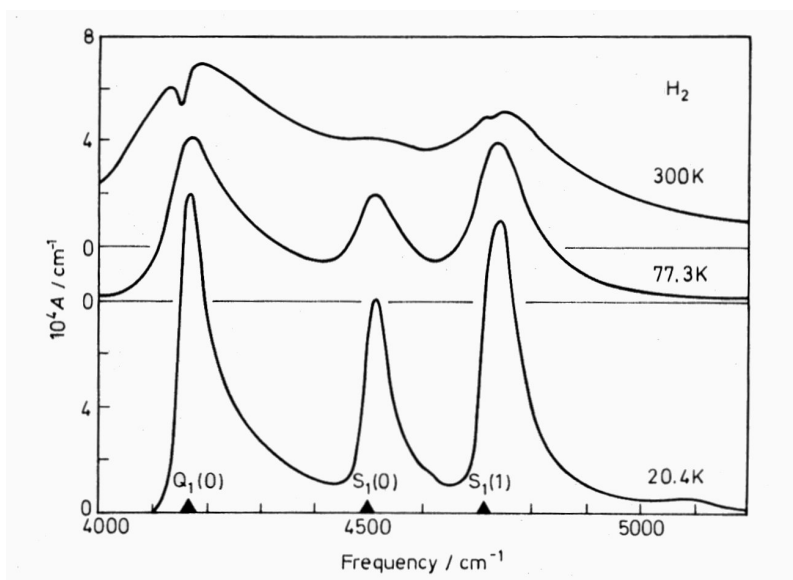


Figure 3.5: Spectra of the fundamental transition of H_2 at 220 psi for different temperatures

In figure 3.5 we see the spectra of the fundamental hydrogen transition at high pressure. We use the standard spectroscopic notation $X_{\Delta\nu}(J)$ to name the different peaks. X stands for the change in J and takes here the values Q for $\Delta J = 0$ and S for $\Delta J = 2$, J is the rotational quantum number of the initial state and $\Delta\nu$ shows the change of the

vibrational state. We observe that the Q-branch is split into two characteristic maxima, which is due to interference of dipole moments induced in successive collisions [31].

The transition lines are very broad which is a consequence of the short lifetime of the dipole moment and the Heisenberg uncertainty principle. At lower temperature the collision duration is longer and therefore the width of the lines decrease as can be seen in figure 3.5.

The pressure induced absorption is due to collisions of two or even more molecules. An absorption due to a binary collision is proportional to the square of the particle density, a ternary collision accordingly to n^3 and so on. It has been shown, that in our pressure range the cubic term contributes less than 7% to the total absorption and therefore we can assume a quadratic dependance on the particle density[30].

It shall be noted, that in a binary collision also both molecules can perform a transition with the absorption of a single photon. Even though this double transitions are of more importance in the overtone bands, they are also present in the fundamental transition, but are not apparent because of overlapping by stronger peaks [5].

3.3 Fourier Transform Infrared Spectroscopy

3.3.1 Functional Principle

The most common tool today for infrared spectroscopy is a fourier transform infrared spectrometer (FTIR). To obtain an absorption spectra the absorption has to be measured dependent on the wavelength.

The main part of an FTIR spectrometer is a Michelson interferometer. Using interference effects a Michelson interferometer can filter certain wavelengths out of a continuous spectrum. As can be seen in figure 3.6 the incoming beam is split into two parts at a beam splitter. Both parts return to the beam splitter after traveling to a mirror and being reflected back. Because one of the mirrors is movable the traveled

distance of one part can be changed.

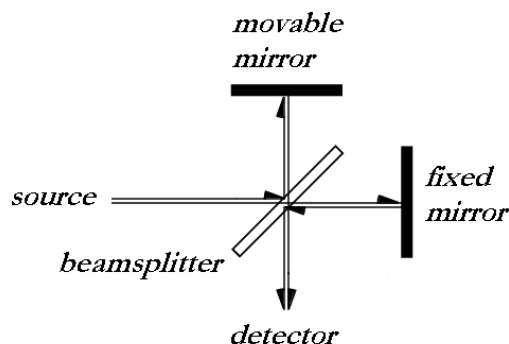


Figure 3.6: A classical Michelson interferometer

At the beam splitter both parts of the beam recombine and split again. Only the recombined beam which is directed to the detector has to be considered in the following. The recombined beam is a sum of both parts of the splitted beam, which traveled different paths to arrive at the detector. Because of the different pathlength a phase shift between both signals arises. According to their phase shift both parts interfere either positively or negatively (cf. figure 3.7). So if the mirror is moved linearly, the detector signal will change sinusoidally.

In a FTIR spectrometer a silicon carbide rod is used as a light source, which is heated electrically and emits infrared radiation with approximately the spectral behavior of a black body. We obtain a more complicated interferogram than for monochromatic light, which is shown in figure 3.9 (a). This always shows a characteristic center burst, which is due to the fact, that at zero phase shift all waves interfere constructively, regardless of their wavelength. At all other phase shifts some waves pass the interferometer constructively and some destructively, so that the signal strength averages out.

To obtain a spectrum from the interferogram, it has to be analyzed of which frequencies it consists and to which amount. This spectral decomposition of the interferogram is done by a Fourier transform. While the original light signal exists in the time domain,

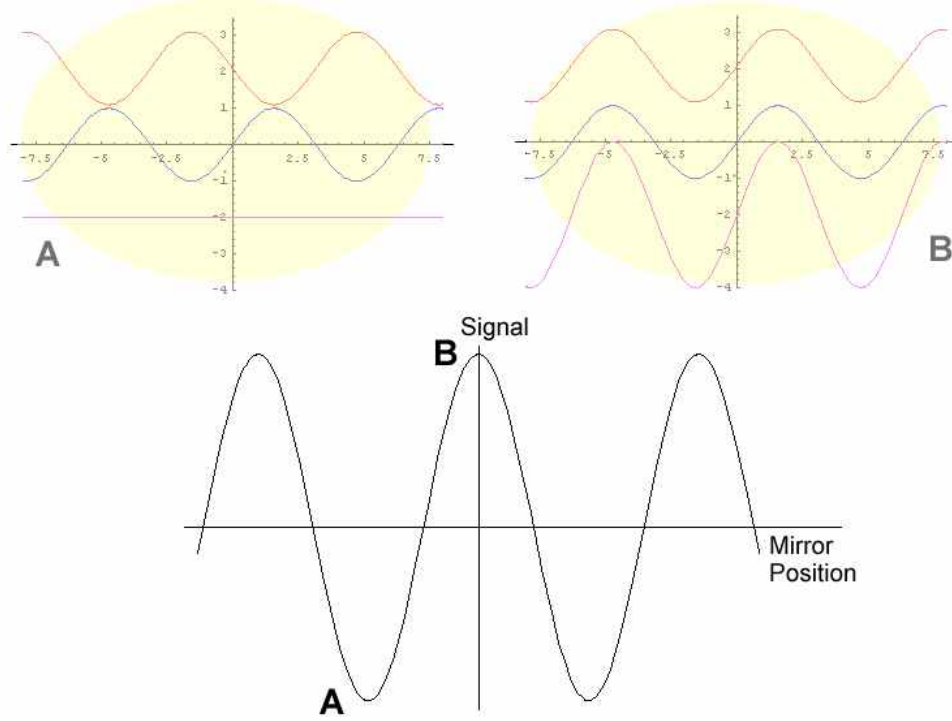


Figure 3.7: The lower figure shows the signal in dependence of the mirror position. If the mirror position equals a pathlength difference of multiple wavelengths, the interference is constructive as shown at point B. Figure B shows the according waves over time and their sum. If the mirror position is half a wavelength, the interference is negative as can be seen in fig. A.

the Michelson interferometer transferred that signal in the space domain, depending on the position x of the mirror. The Fourier transform now transfers that signal in the frequency domain with

$$f(\omega) = FT[f(x)] = \frac{1}{\sqrt{2\pi}} \int_{-\infty}^{\infty} f(x) e^{i\omega x} dx \quad (3.13)$$

The direct transition from the time domain to the frequency domain is not possible, because the time domain cannot be observed due to the high frequencies of the light waves. Therefore the Michelson interferometer is necessary to make the signal observable. A typical spectrum in the frequency scale can be seen in fig. 3.9.

3.3.2 Experimental Considerations

The spectrometer used in this work is a Thermo Nicolet Magna-IR 760. Illustration 3.8 shows a top view of the spectrometer interior and the path of the beam inside the spectrometer. The beam is produced by the light source (1), passes the aperture (2) to adjust its intensity and then enters the interferometer (3). The beam splitter used in the interferometer is a thin silicon layer enclosed in KBr. After that the beam passes the sample (4) in transmission and finally arrives at the detector (5). The beam is redirected several times by concave metal mirrors, so no lenses are used to avoid chromatic aberrations. To align all optical parts of the system a He-Ne laser is used. The whole spectrometer is purged with nitrogen gas¹ to reduce the amount of IR-active molecules in the beam path.

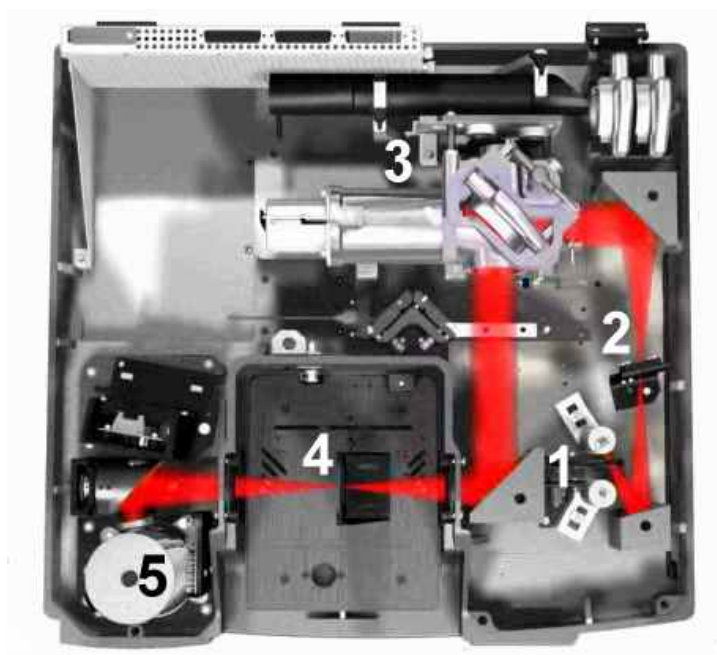


Figure 3.8: Overview of the beam path in the spectrometer. (1) Light source, (2) Aperture, (3) Michelson interferometer, (4) Sample chamber, (5) Detector

In this experiment a MCT (mercury cadmium telluride) detector is used. MCT is a semiconducting material, where an IR photon can excite an electron over the band

¹dry air is used instead, if the nitrogen supply fails

gap. The so increased conductivity is measured. To avoid thermal excitations the detector has to be cooled by liquid nitrogen. The observable range for our system with an MCT(A) detector is between wavenumbers from 600 cm^{-1} to 5000 cm^{-1} .

When a spectrum is taken the detected voltage as function of the wavenumber is measured. But this function indicates not only the properties of the sample, but also of everything in the beam path and - more importantly - the sensitivity function of the detector and the radiation properties of the source. Therefore insights in the absorption of the sample are achieved by a difference spectrum. For this first a reference spectrum of the empty chamber is taken as it can be seen in figure 3.9(b). The characteristic shape of the curve is mainly due to the sensitivity of the detector. IR absorption of molecules in the pathway produces mostly sharp negative peaks, as it can be seen in figure 3.9(c), where the sample has been introduced in the sample compartment. Those spectra are called single beam spectra.

The absorption characteristics of the sample are computed if we subtract the single beam of the empty chamber from the single beam of the sample, creating a difference spectrum as displayed by 3.9(d).

The absorption process is described by the Lambert-Beer-Law, which states, that the intensity of a light beam is absorbed exponentially in the material with

$$I(\lambda) = I_0 e^{-A(\lambda)} \quad (3.14)$$

Here I is the intensity after the absorption, I_0 the initial intensity and A the absorbance² which depends on the wavelength λ . In a reference spectrum the absorption of the empty system A_R is measured, in a sample measurement, the absorption of the sample *and* the empty system is measured. To obtain the absorption of the sample A_S , the

² $A(\lambda)$ describes the absorbance of the whole sample, which would factor in the pathlength of the beam in the material, the concentration of the material and the absorbance coefficient. Though no benefit would be gained here, these details are omitted.

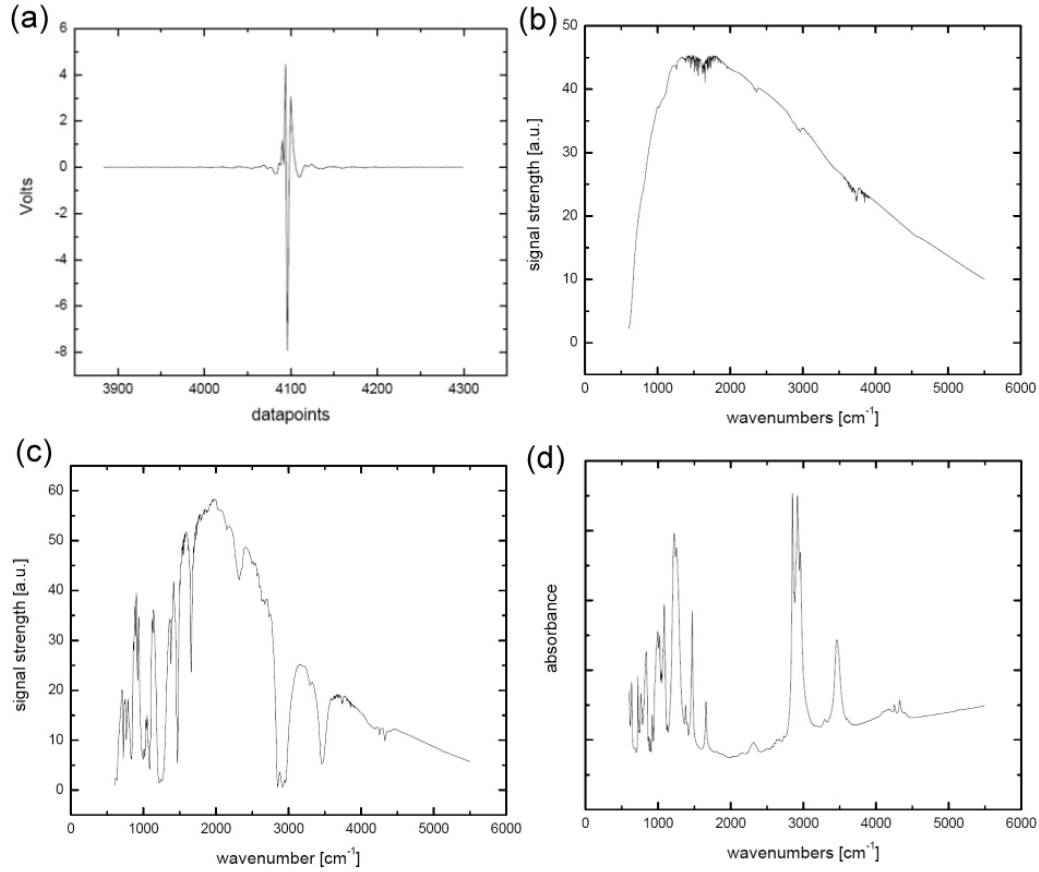


Figure 3.9: Examples of spectral data. (a) shows the interferogram obtained at an empty cell, (b) shows the Fourier transform of that interferogram, also called a single beam, (c) shows the single beam spectrum of sodium dodecyl sulfate (SDS), a surfactant used in the preparation of nanotubes, (d) shows the absorbance spectrum of SDS, computed as difference from b and c

following computation has to be made:

$$\begin{aligned}
 \ln \frac{I_R}{I_S} &= \ln \left(\frac{I_0 e^{-A_R}}{I_0 e^{-(A_R+A_S)}} \right) \\
 &= \ln \left(e^{-A_R} \right) - \ln \left(e^{-(A_R+A_S)} \right) \\
 &= A_S
 \end{aligned} \tag{3.15}$$

So in order to subtract two single beams the logarithm of the ratio has to be taken instead of a simple subtraction.

The quality of a spectrum is determined by the amount of noise and the disturbance by known effects. The amount of noise can be controlled by averaging over several single

measurements. While in general noise is decreased by the number of measurements with $\propto \frac{1}{\sqrt{N}}$, not all noise is really random and will cancel out by taking averages. Therefore the noise level cannot be reduced infinitively by just taking long averages. In this work a spectrum is usually averaged over 1000 measurements.

Furthermore not all absorbances seen in a spectra are due to material present in the sample compartment. As can be seen in the single beam of an evacuated chamber in fig. 3.9 (b), there are several sharp peaks of absorbance visible, most notable those around 1600 cm^{-1} , 2350 cm^{-1} and 3800 cm^{-1} . These peaks are due to gas phase water and CO_2 , which have a very big IR cross section, so that even small amounts are visible in IR. These peaks do not vanish when the chamber is evacuated, because these molecules are present in the part of the beam path, which is inside the spectrometer even though this area is purged. Because the amount of this peaks are always changing slightly, these peaks also occur in difference spectra.

Chapter 4

Experimental Setup

Because the experiment was designed and built during this work, the setup of the experiment changed several times during this time. Here described is the final state of the setup, omitting additional equipment, like a device for the introduction of gaseous water or a mass spectrometer, which have not been used in this experiment.

4.1 High Pressure Cell

The experiments in this work are partially done under high pressure conditions, so the experimental setup centers around a high pressure cell. The cell has been obtained from *Specac Limited* and can be operated with pressures up to 1000 psi. A picture of the cell is shown at fig. 4.1. The cell consists of stainless steel and has two ZnSe windows for transmission of the IR beam. The sample holder can be removed from the cell completely and can be loaded with samples up to a diameter of 13mm, which are hold in place by two screws. These screws limit the actual aperture at the sample to 11 mm. In the case of contamination the ZnSe windows can be disassembled for easier access to the inside of the cell and the windows itself.

The cell is built in the sample compartment of the FTIR spectrometer described in chapter 3.3.2. To avoid room air in the optical path, aluminum tubings have been custom built to bridge the distance between the cell windows and the beam outlet at the sample compartment. These tubing are sealed at the cell with Si rings and are purged from the inside of the spectrometer.

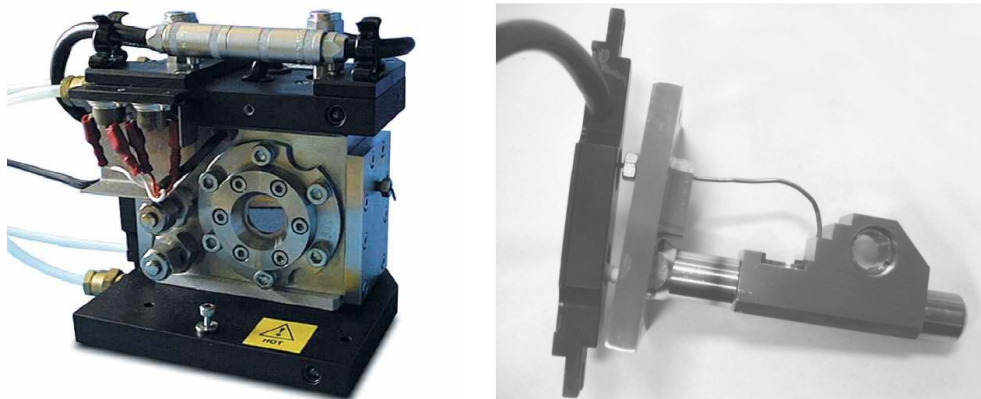


Figure 4.1: (left) Side view of the high pressure cell, (right) The sample holder

4.2 High Pressure

A schematic view of the setup is shown in figure 4.2. Not shown here, the actual lab setup contains two identical systems, which share the same pumping station, gas bottle and water cooling. Because this systems are shared, the tubing allows technically a gas exchange between both cells. Therefore special care was taken in the experimental schedule of both systems to avoid possible gas flow between both systems. All data presented here has been taken in the same cell.

To provide hydrogen the cell is connected over a regulator (V-2) with a gas bottle of 6000 psi, which according to the provider contains 2.4 ppm H_2O and 0.6 ppm O_2 [32]. The pressure in the chamber can be measured by a pressure gauge directly attached to the system (G-3) or one attached to the regulator on the gas bottle (G-2). If the gas volumes of both cells are connected at high pressure, the difference between the readings at the valves of each system differ by up to 100 psi, which makes the reading accuracy of ± 25 psi neglectable.

The hydrogen can be released by opening the regulator V-4 and is then emitted in the atmosphere. The small cell volume of 80 ml prevents dangerous hydrogen levels in the room air. To avoid possible damage due to overpressure, a burst disk has been added to the system, which will be destroyed by overpressure and then release the gas.

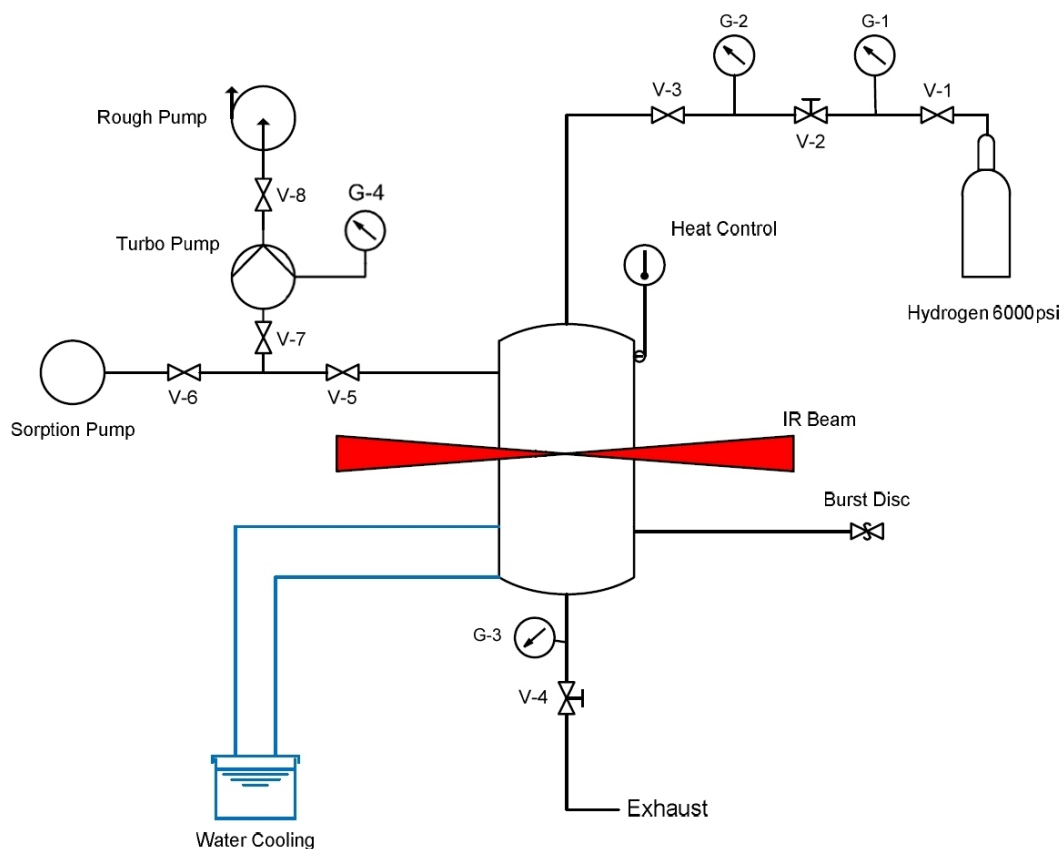


Figure 4.2: Schematic of the experiment setup. Valves and gauges are numbered for later reference.

High pressure tests have shown, that at around 1000 psi the cell is losing between 30-50 psi in 24h. At delivery the cell showed a bigger amount of leakage, which could be reduced by replacing the original O-rings at the tube connectors with ones of a different size. The remaining leakage still requires a connection to the gas bottle to be open to maintain a constant cell pressure for long time measurements

4.3 Vacuum

To provide vacuum in the cell, a turbo molecular pump is connected to the system. To enable the turbo pump to work efficiently, a rough pump and a sorption pump are added as auxiliary pumps.

A turbo molecular pump is based on imparting momentum to an incoming gas molecule and so transfer it from the inlet toward the outlet. Therefore it consists of a alternating series of high-speed rotating blades (rotors) and fixed blades (stators). The blades of the rotor and of the stator are angled in opposing directions as can be seen in fig. 4.3. A gas molecule is hit by a rotor blade and accelerated. Because of the tilting of the blades, it will preferably hit the lower side of the blades of the next stator and so is moved towards the outlet. The compression towards the outlet is so increased.

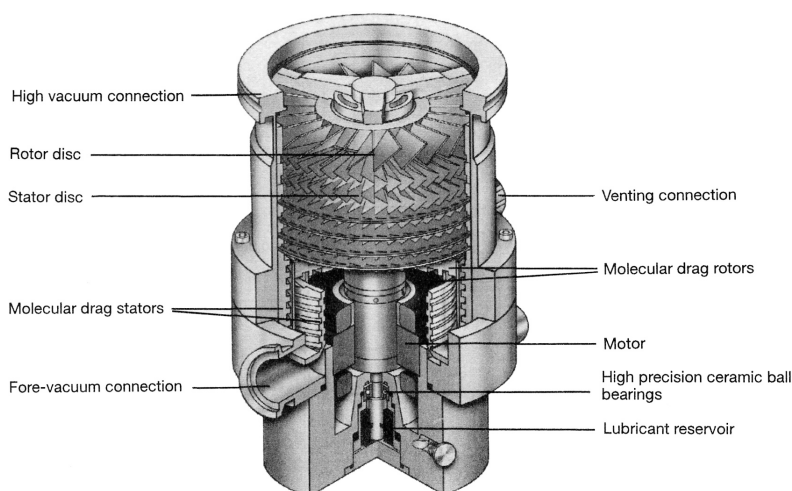


Figure 4.3: Cross section of a turbomolecular pump.

In order to transfer a gas molecule from one blade to another, the mean free path for that gas has to be higher than the distance between two blades. Because the pressure towards the outlet is increasing, the rotor/stator stages become smaller and smaller towards the outlet to keep the blade distance smaller than the mean free path. Pumping against room pressure at the outlet would require infinitely small stages. To avoid that a rough pump is backing up the turbo pump, by providing a fore-vacuum at the outlet. The rough pump used here is a rotary valve pump. While a running turbo pump emits no oil in the vacuum system, because magnetic bearings are used on the high vacuum side, the rotary valve pump needs full lubrication. To prevent back streaming of oil from the rough pump, the valve V-8 has to be closed if the turbo pump is not running. After the turbo pump is shut down, it is automatically vented with room air, to prevent

lubricant from the bearing on the low-vacuum side to diffuse into the chamber. Therefore the pump has to be disconnected from the chamber by closing valve V-7 before shut-down.

Because the quality of the vacuum depends on the cleanness of the turbo pump, best results are obtained, if the (preferably baked) turbo pump is kept constantly running. Because exposure to room pressure of the turbo pump inlet at full speed can damage the turbo pump, a sorption pump was installed to achieve a low vacuum before using the turbo pump. If the sorption pump could not be used due to lack of liquid nitrogen, the turbo pump had to be stopped and restarted to be able to pump room pressure at starting conditions.

To measure the pressure at vacuum conditions a ionisation gauge (G-4) was used. Ionisation gauges cover the pressure range from 10^{-5} torr to 10^{-12} torr and rely on the fact that a beam of electrons will ionize molecules on their way [6]. Therefore a tungsten filament is heated to emit electrons, which then ionize molecules on their way through the gauge. The so produced ions are collected and the ion current is proportional to the molecular density. The tungsten filament would burn out at ambient conditions, so the gauge may only be initiated in appropriate vacuum conditions.

The vacuum achieved at the gauge was up to 10^{-7} torr with a baked system and 10^{-6} torr otherwise. Because the gauge is connected to the turbo pump, the pressure of the pump is measured instead of the pressure in the cell. The actual cell pressure can be up to two orders of magnitude higher.

4.4 Temperature Control

To allow better vacuum conditions, the cell walls and the sample holder can be baked individually. Therefore a WEST 6100+ power controller allows settings for the cell temperature and the sample temperature. The temperature for both are measured

by thermocouples. The maximum temperature for the cell is 200°C and 800°C for the sample, but temperatures over 700°C reduce the heater life time [33]. Because hydrogen can damage stainless steel at such high temperatures, all baking was always done under vacuum conditions.

The heating speed was set to roughly 90 min from room temperature to 700°C. The cooling process could not be influenced and takes 3-4 hours from 700°C to room temperature. Water cooling of the top and bottom plate of the cell prevent excessive heat at the cell electrics and the spectrometer sample compartment.

Chapter 5

Experimental Results

5.1 Hydrogen Measurements - Preface

It was tried to measure the interaction of hydrogen with carbon nanotubes under high pressure conditions. Because no interaction could be detected, the preparation method for the samples has been enhanced several times to allow the deposition of more nanotubes while maintaining a high transmission signal to allow low-noise measurements.

For a better overview the various preparation methods and their spectroscopic investigation is discussed first in section 5.2. The results of the interaction with hydrogen for all samples is then presented in section 5.3.

5.2 Sample Measurements

5.2.1 Samples on KBr Substrate - Preparation

Samples have been prepared with two different preparation methods, here referred as method A and B. For a better overview I will first describe both methods and then discuss the results in section 5.2.2.

Type A

The goal of the sample preparation was to provide a uniform, stable film of SWNTs on the substrate. Because the sample holder is designed to take up circular samples of 13 mm diameter, the substrate was chosen to be KBr, which can be pressed into pellets of the according size. 200 mg of KBr were pressed with up to 6 tons pressure to produce

pellets which transmitted around 90% of IR-signal intensity.

To produce a thin film of nanotubes from the solution, the liquid was filtered through filter paper by suction filtration and afterwards rinsed with deionized water until the filtered water showed no soap bubbles due to SDS anymore. The filter paper used was mixed cellulose ester (MCE) filter paper with a pore size of 200 nm (in later experiments 220 nm).

To put the nanotube film from the dried filter paper on the substrate, the filter paper was put face-down on the KBr pellet and moistened with a drop of water to improve the contact. The so sandwiched nanotubes were left overnight in a vacuum oven at 70°C and 80 torr with a pressure of 1 kg on it to allow a good contact between the nanotubes with the substrate.

The filter paper was removed by flushing the sample with acetone thoroughly. The KBr takes no visible damage from that treatment. To evaporate the acetone completely the sample was again put in the vacuum oven at 70°C and 80 torr for several hours.

After trying different amounts of nanotubes, which gave no infrared signal, two samples have been made from 200 ml respectively 400 ml of a 4 mg/l solution. Factoring in the diameter of the complete filter paper and diameter of the KBr substrate this leads to an amount of 0.11 mg respectively 0.22 mg on the sample. Due to a failure the assignment to the amount was lost, and so the samples are named KBr-X and KBr-Y with no correlation to the sample amount.

As shown in figure 5.1 the nanotubes are clearly visible as a black film on the substrate.

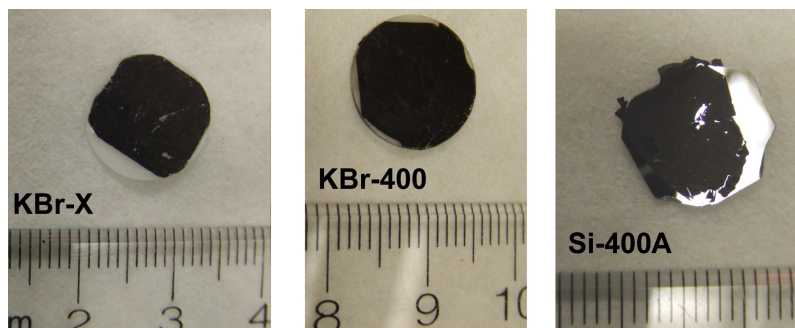


Figure 5.1: Photographs of different samples. The scale is in cm. The nanotube film of Sample Si-400A was damaged by mounting in the sample holder.

Type B

Because method A was very time consuming and contaminated the sample, a new method to apply the sample to the substrate was developed.

The nanotubes are transferred from the suspension to the filter paper as in method A. Then the filter paper with the nanotubes on it is put in an acetone bath, which dissolves the filter paper. The nanotube film stays intact and is floating on the acetone from where it can be picked up with the KBr pellet. To prevent the dissolved filter paper from drying on the sample after removing it from the bath, the sample is put into several baths of fresh acetone before the final removing.

Afterwards the sample is dried in the vacuum oven under the usual conditions (70°C, 80 torr) for several hours.

The integrity of the floating film without support by a substrate showed the strong cohesion forces of the nanotubes. To use this strength, it was tried to pick up the floating films with a ring of stainless steel, supporting it on the edge but avoiding any substrate in the beam. Several attempts did not achieved to pick the film up without tearing it apart, so this approach was discarded.

Four samples have been made with 50, 100, 200 and 400 ml of a 4 mg/l solution filtered. For the 200 ml and 400 ml sample, the filter paper prepared for the samples

of method A has been used. Factoring in the size of the whole filter paper and the size of the KBr substrate this leads to amounts of 0.026 mg, 0.052 mg, 0.10 mg and 0.21 mg on each sample. The produced pellets are called KBr-50, KBr-100, KBr-200 and KBr-400 according to the amount of suspension used.

5.2.2 Samples on KBr Substrate - Results

Comparison of both Sample Types

Spectra of all samples have been taken under vacuum conditions with reference to an empty chamber. The results are shown in figure 5.2 and 5.3. All difference spectra taken, showed a tilted or curved baseline. Therefore all spectra shown here are baseline corrected.

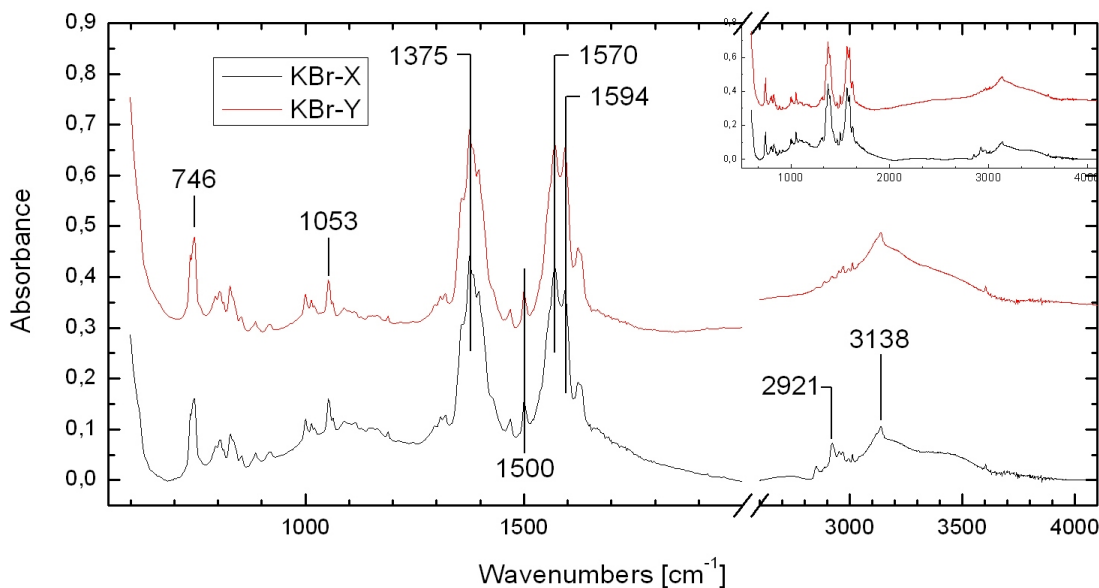


Figure 5.2: Absorbance spectra of KBr-X and KBr-Y. Two sections are shown in detail while the complete spectra can be seen in the inset. Both spectra are shown at the same scale, but are shifted vertically for better display. The major features are labeled with the according wavenumbers.

It can be seen that each preparation method generates a reproducible spectrum, but the spectra of each method are very different. The fact that KBr-X and KBr-Y have been made from the same filter paper as KBr-200 and KBr-400 shows that the

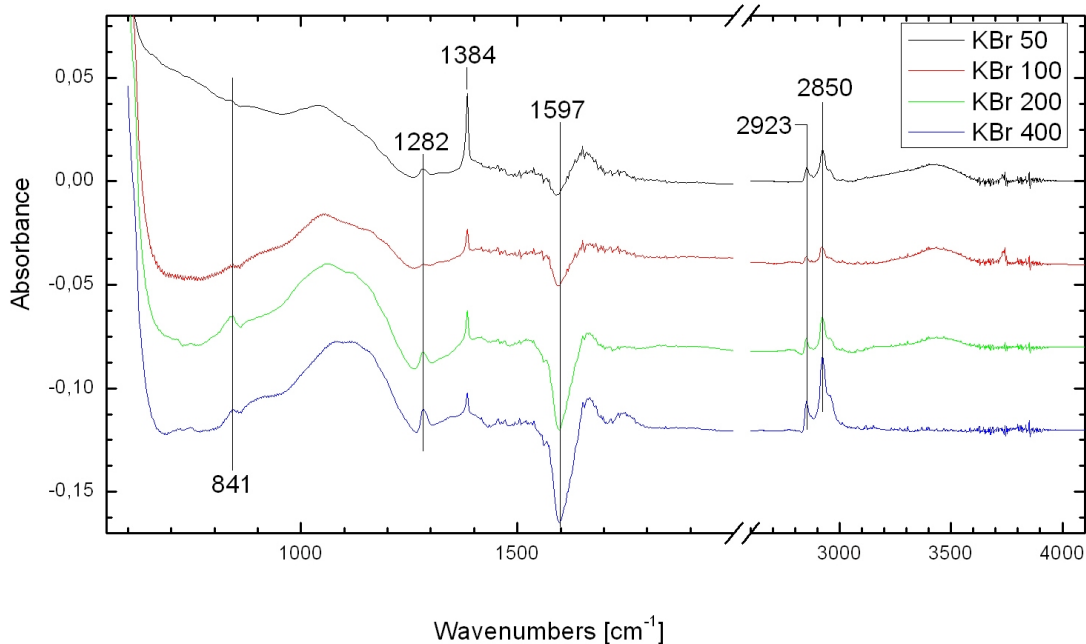


Figure 5.3: Absorbance spectra of KBr-50, KBr-100, KBr-200 and KBr-400. All spectra are shown at the same scale, but are shifted vertically for better display. The major features are labeled with the according wavenumbers.

difference in the spectra is caused by the transfer process from the filter paper to the substrate.

If we compare our results to the data from [3] shown in section 2.4, we see no agreement. The fact, that the peaks in both preparation methods do not match with each other nor with the literature, leads to the conclusion, that the peaks observed on our samples are not due to the nanotubes on our sample, but rather from contaminants on the sample.

If we compare the intensity of the peaks from samples in figure 5.2 (type A) and figure 5.3 (type B), we see that the major features of sample type A (1375 cm^{-1} , 1570 cm^{-1} and 746 cm^{-1}) are by a order of magnitude higher than the main features of type B (1597 cm^{-1} , 1384 cm^{-1} and 1281 cm^{-1}). This indicates that - even if both preparation methods are contaminating the sample - method B is the cleaner preparation method and thus preferable.

It can be seen, that the samples produced with method A also show the same peaks as samples produced with method B, even though the A spectra is dominated by other features. A detailed look at the spectra of type A shows, that there are peaks at 1384 cm^{-1} , 841 cm^{-1} and slightly shifted at 1282 cm^{-1} . Furthermore the broad peak from 1000 cm^{-1} to 1200 cm^{-1} is also present in both spectra. Figure 5.4 shows a direct comparison of KBr400 and KBr-X. The spectra of KBr400 is magnified ten times to allow a better comparison.

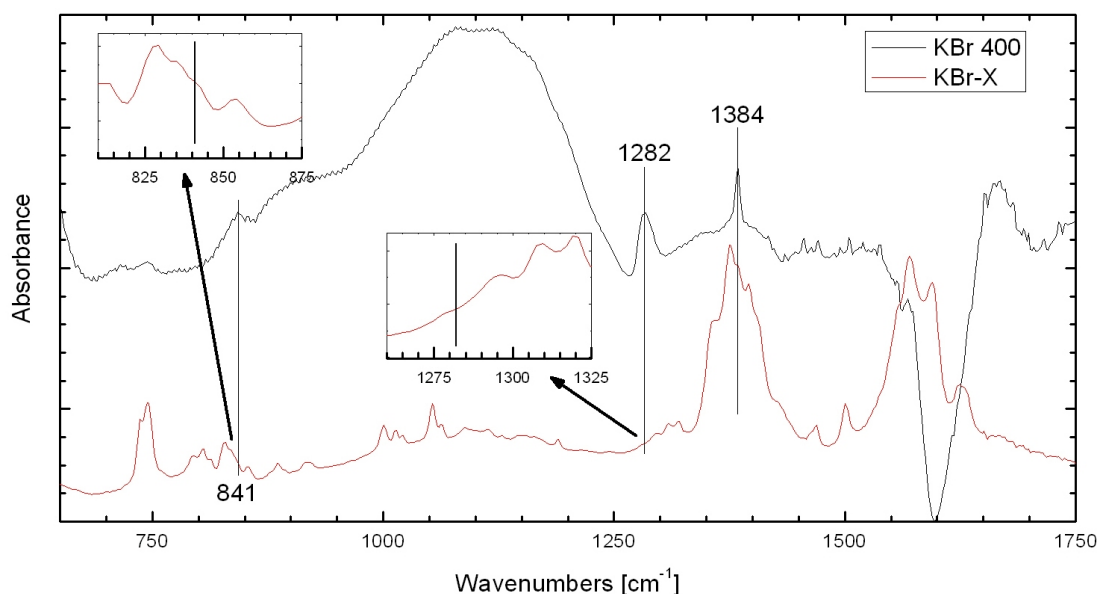


Figure 5.4: Spectra of KBr-X and KBr 400 in direct comparison. The spectra of KBr-400 is magnified with a factor of 10. For finer details the peaks at 841 cm^{-1} and 1281 cm^{-1} are magnified. The peaks of the KBr400 sample can also be found in the KBr-X sample.

Scattering

The spectra shown in the figures 5.2 and 5.3 are baseline corrected, which allows better display and comparison, but also omits additional information. The uncorrected spectra for samples made by method B are shown in figure 5.5. It can be seen that the absorption at low wavenumbers increases with the amount of nanotubes.

Because baseline shifts can also be caused by several external parameters (e.g. temperature shifts), we can not distinguish between a broad absorption and a random baseline shift. So an exact quantitative statement about the dependence of absorption due to the amount of nanotubes can not be made. If we compare the absorbance in figure 5.5 to the uncorrected spectra in the literature (fig 2.5), we see that the claimed electronic contribution from [3] has a minimum around 1600 cm^{-1} while our spectra has increasing absorbance with lower wavenumbers. Therefore our feature is not the claimed electronic transition.

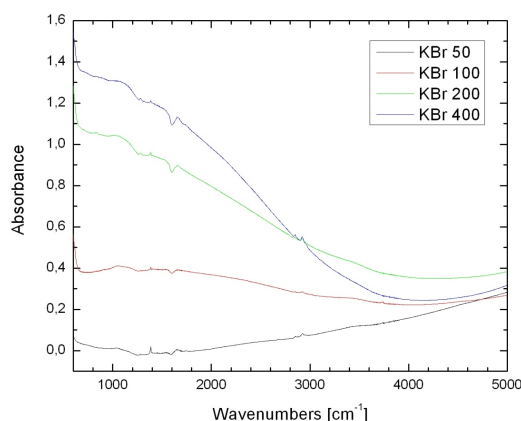


Figure 5.5: The uncorrected spectra from the samples of method B. All spectra are on common scale. At low wavenumbers the absorbance increases with the amount of nanotubes.

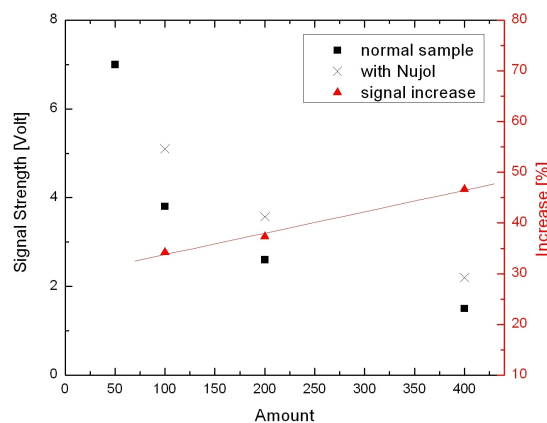


Figure 5.6: The intensity of the interferogram for different samples after and before they were treated with Nujol. The data marked in red show the relative increase in transmission for all samples in %.

A possible reason for the absorption can be scattering on the individual tubes or on bundles of tubes, which would explain the scaling with the amount of sample. As illustrated in figure 5.7 scattering occurs at each interface of two materials with different refractive indices.

To investigate the scattering behavior a few drops of a mineral oil with a refractive index of 1.44, called Nujol¹, have been dropped on the sample. The oil replaces the vacuum between the individual bundles of nanotubes. Because the refractive index of

¹Provided from AlfaAesar

the interstices matches now more closely the one of the sample material, the scattering is reduced.

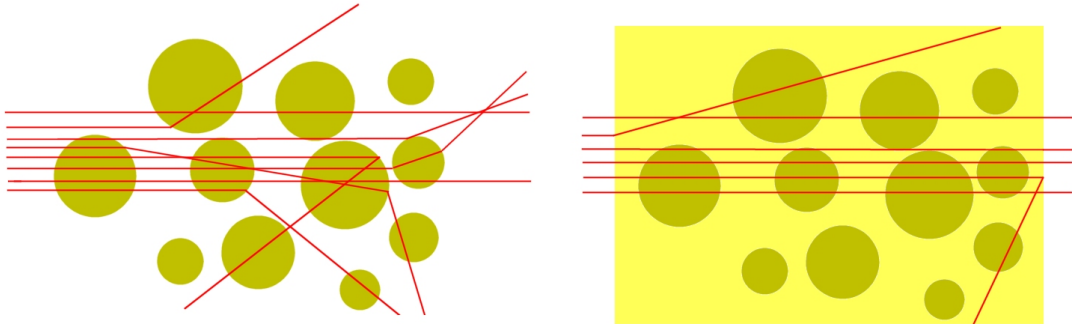


Figure 5.7: (left) Light is scattered at all interfaces with different refractive indices. (right) If a liquid of similar refractive index is filled between the particles, less the light is scattered.

A spectrum was taken before and after the treatment with Nujol to compare the amount of absorption. The maximal amplitude of the interferogram was measured to summarize the total transmission. Figure 5.6 shows a plot of the amplitude of the samples with and without Nujol for the different amounts of sample used. It can be seen, that the use of Nujol increases the transmission by 35-45%. The increase of transmission relative to the total signal is also plotted and increases with the amount of sample. The reason for that is, that the absorption due to scattering becomes more dominating for higher amounts while at lower amounts other absorption effects have to be considered.

Because the hydrogen interaction with these samples was below the detection limit (cf. section 5.3), higher amounts of SWNTs are necessary. As can be seen from figure 5.6, the increase of sample amount lowers the transmitted signal, which limits the maximum amount. The use of Nujol to increase the transmission has the disadvantage of introducing additional features to the spectrum, of blocking the access of hydrogen to the nanotubes and of being not stable at baking. Therefore the further use of Nujol was refrained in this work.

When evaluating the transmission intensity the changing sensitivity of the detector has to be taken into account, which gave variations of up to 20% in the intensity for measurements on the same sample on different days. Furthermore the nanotube amount applied to each substrate cannot be calculated easily, because the weight values given in section 5.2.1 assume a complete coverage of the 13 mm disk. In fact the disks are never completely covered (as can be seen in figure 5.1), which can reduce the actual amount of sample in the beam at high apertures, which are usually used in this work due to the high absorption of the sample material.

The amount of nanotubes which can be applied to a sample is limited by the high absorption observed. As can be seen in figure 5.6 the signal strength decreases for high amounts. Analysis of the data shows, that the signal decreases anti proportional to the amount of nanotubes as can be seen in figure 5.8. To estimate the signal strength at higher amounts a curve according to $\text{Signal} = a (\text{Amount})^{-1}$ has been drawn in figure 5.9. The factor a has been taken from the slope of curve in fig. 5.8, which has been fitted to values of the four KBr samples.

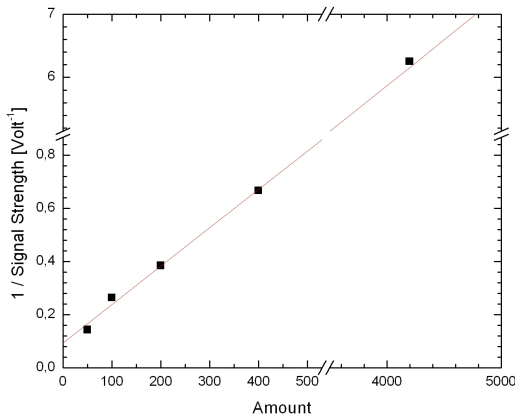


Figure 5.8: The intensity of $(\text{signal})^{-1}$ is plotted over the amount. The point at 4200 represents the Sample SiMax1 (cf. sec 5.2.3). A linear fit of the first four values is shown. It can be seen, that the signal strength of SiMax1 also lies close to the the fitted curve.

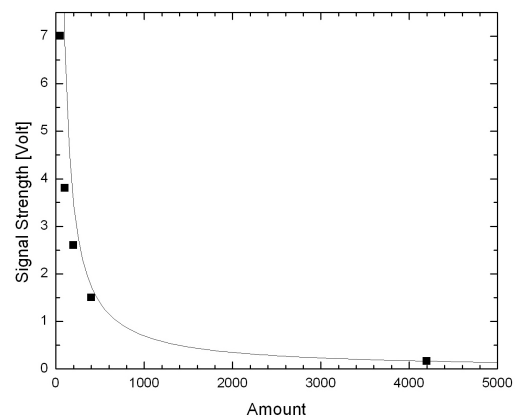


Figure 5.9: Plot of the signal strength over the amount. A function $\text{Signal} = a (\text{Amount})^{-1}$ is drawn into the curve with the parameter a taken from the slope of figure 5.8.

From figure 5.9 we can estimate the maximum amount of sample possible which would still give sufficient signal. If we assume a necessary signal strength of 0.1 to distinguish the sample from the noise, the maximal sample amount would be 7000 ml of the used solution on the filter paper which equals 3.7 mg on the substrate. Considering the uncertainties about the noise in the system and in the absorption behavior of the samples, the estimation can be made, that the amount of sample can be increased by at least one order of magnitude to still allow transmission.

Peak Assignment

To identify the peaks in both type A and type B samples spectra of the following samples have been taken to identify possible contaminations.

- Filter paper was dissolved in acetone and then a KBr pellet was first submerged in the solution and then dried in vacuum, evaporating the acetone with only filter paper remaining.
- SDS (sodium dodecyl sulfate) in powder form was pressed on a KBr pellet.
- A plain KBr pellet.

The according spectra can be seen in the appendix A.

Comparison with the SDS and the filter paper sample showed, that the peaks observed in type A and type B spectra are not due to residua of those contaminants. Comparison with an acetone spectra from [34] showed also no agreement in the peak positions, so that residua of acetone can also be ruled out.

The comparison with the KBr spectrum showed, that the sharp peak at 1384 cm^{-1} is also present on the plain KBr pellet. Measurements of several KBr pellets showed that this peak can always be detected even though it may vary in size. Because a pure KBr pellet has no sharp spectral features in the IR [35], this feature has to be attributed to a contamination of the pellet either existing in the powder itself or applied when

pressing into pellets.

The group of peaks from 2850 cm^{-1} to 3000 cm^{-1} are hydrocarbons which are always present in the spectrometer. The spectra shown here are difference spectra, so it can be deduced, that hydrocarbons are present on the sample. Because a hydrocarbon signal can also be found on a plain KBr pellet and its amount does not scale with the amount of carbon nanotubes (as can be seen in fig. 5.3), it is believed that the hydrocarbons observed here are not specifically attached to the nanotubes.

While only the A samples show a sharp peak at 3138 cm^{-1} , both sample types show a broad peak from 3000 cm^{-1} to 3600 cm^{-1} , which is in the typical range of -OH groups. This peak has also been observed on plain KBr pellets and can be assigned to adsorbed water in the material. It has been shown, that baking up to 150°C for 1-2 hours can not remove this peak. This can be explained by water being absorbed inside the porous material, which increases the necessary energy for outgassing and thus slows down the evaporation process.

When baking to higher temperatures with a KBr substrate, a film on the inside of the cell windows has been detected. This was assigned to the sublimation of KBr particles, which condensed on the window material, which could not be heated to more than 150°C . To avoid this problem, further samples have been prepared on thermally stable Si.

As mentioned above due to the strongly curved baselines (compare figure 5.5) a baseline correction had to be made in all shown spectra. The baseline correction was set by hand to follow the broad shape of the spectrum. This method produces a flat baseline while maintaining all sharp features of the spectrum. This method is not accurate for very broad features which can be easily changed in height by the baseline correction. Because the uncorrected baselines show the strongest curvature for low wavenumbers, the biggest errors due to baseline corrections appear at low wavenumbers.

The "negative peak" in the B-samples at 1597 cm^{-1} as shown in figure 5.3 is an artifact of this effect. Because the spectra are taken with reference to an empty chamber, it is not possible that negative peaks appear. Therefore this peak has to be interpreted as the minimum between two broad features on either side of the peak.

Furthermore the exact shape of all broad features at low wavenumbers can not be taken as accurate information, but as a general trend.

It can be summarized so far, that both preparation methods produce the peaks seen in figure 5.3, while method A also has additional features. This suggests, that the features seen in figure 5.3 are more intrinsic to the sample than those of figure 5.2. Some peaks have been assigned to contaminations on the sample, but most features could not be assigned to a specific material. Because the remaining peaks do not scale with amount of sample and do not agree with published measurements about carbon nanotubes [3, 28], it is believed that they are not related to SWNTs but are due to other impurities on the sample.

5.2.3 Samples on Si Substrate

The silicon used for these samples is float-zone Si(111). The silicon has been cleaned prior to use and is passivated with a SiO_2 layer on the surface. The cleaning process is described in appendix B. Because the native oxide layer on the silicon produces an IR signal, all sample measurement have been taken with reference of the empty Si substrate.

Baking

Si substrates have been used to allow higher annealing temperatures than for KBr substrates. High temperature annealing was reported to outgas impurities in the nanotubes [3] and has been shown to remove carboxyl groups, which are blocking the entry ports of the nanotubes and thus are reducing the hydrogen uptake[26].

The silicon samples have been annealed in the high pressure cell under vacuum conditions. The sample holder could be heated up to 700°C while the cell body could only be heated up to 200°C. It has been observed, that annealing at high temperatures coated the cell windows with an absorptive layer. The reason is that at high temperatures molecules are outgassing from the sample material and are hitting the windows, where they readsorb due to the lower temperature of the windows.

To avoid coating of the windows a shield of stainless steel has been built and inserted in the cell before high temperature annealing. To take a spectrum after the annealing the cell had to be opened to remove the shield. To remove possible contaminants introduced by the opening the cell was again annealed for 1 hour at 150°C before finally taking the spectrum.

After a high temperature annealing a coating centered around the position of the sample could be seen on the shield, while no absorption was detected on the windows.

Preparation

The sample preparation method described as method B has been used to apply nanotubes to silicon substrates.

To compare the behavior on different substrates two samples with the amount of SWNTs as on the KBr400 sample have been prepared. To minimize differences in the preparation the samples have been made from the same sheet of filtered nanotubes as the KBr400 sample which equals an amount of 0.21 mg per sample. The nanotubes have been transferred from the filter paper to the substrate with the method B as it is described in section 5.2.1.

Because acetone does not evaporate cleanly and can leave residues on the surface,

one sample was rinsed with methanol after the acetone bath to remove the acetone before evaporation. It is believed that the methanol evaporation leaves less residua. The sample which was additionally rinsed with methanol is called Si400m while the sample which was only rinsed with acetone is called Si400a.

To increase a possible interaction signal of hydrogen on nanotubes, samples with a ten times higher amount have been prepared. To avoid the filtering of large quantities of solution, a high concentration has been used. For that 5.9 mg of nanotubes have been put in a 20ml flask of water with 1wt% SDS. After sonication for 2 hours the black liquid has been carefully poured into the filter apparatus to leave the not dissolved pieces in the flask. The flask has been refilled with water and sonicated for an additional hour until the remaining nanotubes have also been dissolved and then have been added to the filtration. The nanotubes have been transferred from the filter paper to the substrate with method B and afterwards rinsed with methanol. Two samples have been prepared from this filter paper. Both have an amount of 2.1 mg nanotubes on it and are called SiMax1 and SiMax2.

Results

Measurements of the Si400m sample have been taken before baking and after successive baking to 150°C, 500°C and 720°C; sample Si400a was only baked up to 500°C. The according spectra are shown in figure 5.10 and 5.11. The pressure during baking did not rise over 10^{-6} torr.

When comparing the spectrum of the Si400m sample with the spectra of the KBr-based samples (fig.5.3) it can be seen that the negative peak at 1597 cm^{-1} is visible on both sample types but vanishes at baking over 500°C. The sharp feature at 1384 cm^{-1} in the KBr samples can not be found in the Si samples, which confirms that it is caused by the KBr substrate (cf. page 44). The general agreement between the KBr and the Si samples is very low, which indicates, that the features seen here are not intrinsic to

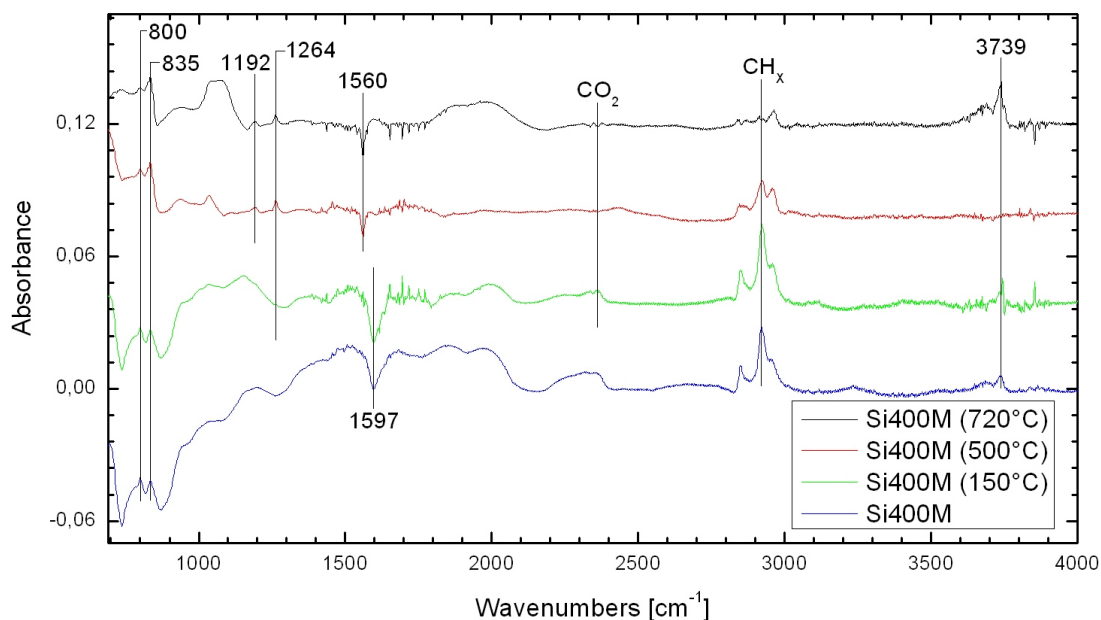


Figure 5.10: Spectra of Si400m after baking to different temperatures. All spectra are at common scale and are shifted vertically for better display.

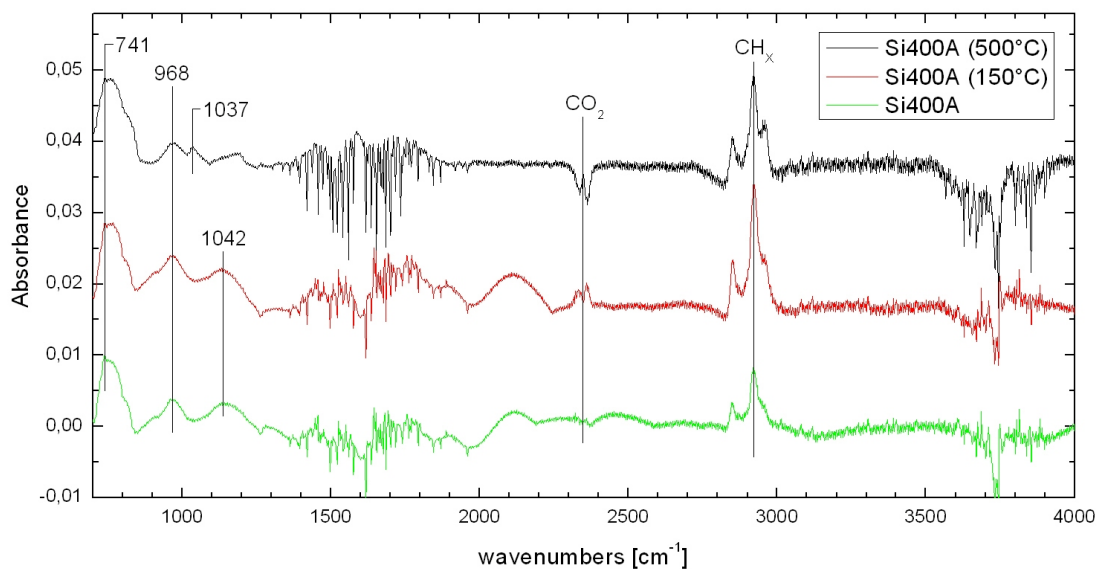


Figure 5.11: Spectra of Si400a after baking to different temperatures. All spectra are at common scale and are shifted vertically for better display. During the measurements the spectrometer was purged with dry air instead of nitrogen, which explains the high amount of water in the spectrum. For comparison of fig.5.10 and fig.5.11 the different scales of both figures have to be taken into account.

the nanotubes and are due to contamination on the sample or in the system.

The spectra shown in figure 5.10 and 5.11 are taken with the empty silicon substrate as a reference, so absorption of the Si should not be visible. Anyhow the signal of the Si substrate can change due to the baking process or due to changes in the sample position, because the Si was removed for nanotube application and then reinstalled. Figure 5.12 shows the single beam of the Si substrate which was used for reference, the single beam of the empty cell and the difference spectrum of the Si400m sample.

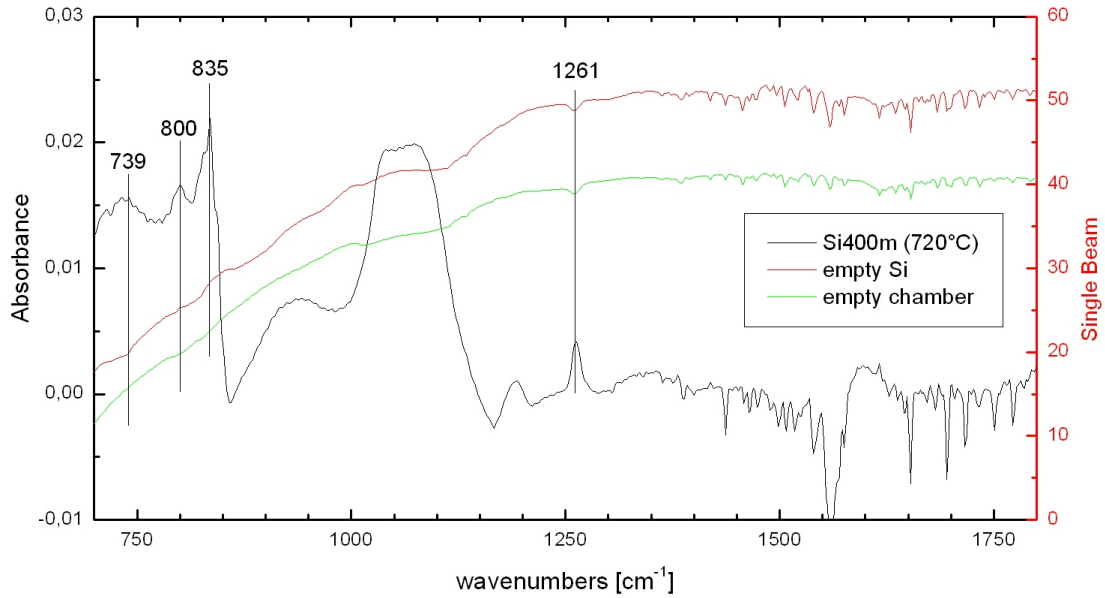


Figure 5.12: The spectrum of the Si400m sample is compared with the single beam of the plain Si and of an empty chamber.

It can be seen, that the feature at 1261 cm^{-1} is also present in the Si measurement and in an empty cell. Therefore it can be said, that the feature in the difference spectra is due to a change in the reference instead of being related to the applied sample

When measuring a sharp feature with a high slope, a small change in the x-axis produces a high change in the y-axis. Therefore the height of sharp peaks can vary in different measurements. As we can see in figure 5.12 the features at 835 cm^{-1} and below always coincide with changes in the slope of the single beam of the empty silicon.

Therefore these peaks in the difference spectrum can be due to small changes in the Si features or in the measurement of those.

The peak at 3739 cm^{-1} in the Si400m spectra, which seems to vary while baking also occurs on the SiMax samples and is explained in that section (page 53).

When comparing the spectrum of Si400m (fig.5.10) to the spectrum of Si400a (fig.5.11), we see that most of the sharp features of the Si400m sample are not present in the Si400a sample. The difference in the preparation method of both samples is the final flushing with methanol to remove the acetone. Because the SiMax sample, which has also been flushed with methanol, shows not the same peaks as the Si400m sample, it is suggested, that these peaks are not due to the interaction of methanol with the nanotubes or from the nanotubes itself.

Several broad peaks below 1400 cm^{-1} are visible in both samples, which can also be found in the samples on KBr substrates. These broad features are at different positions for the different samples and do not coincide with the peaks of the literature [3]. Because the baseline is highly curved in the low wavenumber range, the exact shape of these peaks is not known. The here shown curve represents a baseline correction at the best knowledge but slightly different curves are possible. Furthermore it has been tested, that the shape of the broad peaks does change, when the sample is removed and reinstalled. Because each sample has to be removed at least once for applying the nanotubes, the position of the sample is not identical in the measurement of the spectrum and the reference.

Therefore the broad features can be experimental artifacts and are considered no valid information about the sample.

While all other samples stucked to their substrate, the nanotube film of the SiMax samples stucked to the substrate while being wet, but just layed loosely on the Si after it was dried. The SiMax1 sample was first measured on the Si substrate, then the

nanotube film was carefully removed from the Si and mounted in the sample holder. A piece of the thin film broke off when handling the dried material, so that the measurements without substrate represent a slightly lower sample amount. The SiMax2 sample was directly measured without a Si substrate.

The SiMax samples were also baked up to successively 720°C . Because the spectra of the samples showed no apparent change due to baking only spectra after 720°C are shown in figure 5.13.

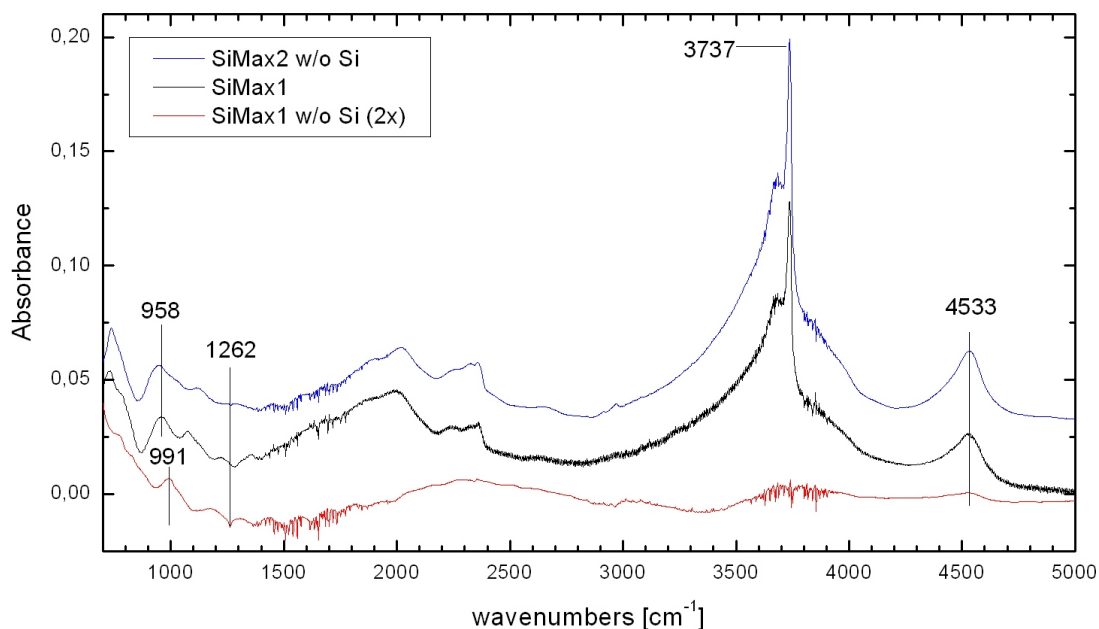


Figure 5.13: Spectra of the SiMax1 sample with and without the Si substrate and of the SiMax2 sample without substrate. All spectra are taken after a baking to 720°C . For better display all spectra are shifted vertically and the spectrum of SiMax1 w/o substrate is magnified by a factor of 2.

The most dominant features in the measurements are a sharp peak at 3737 cm^{-1} and broader and smaller feature at 4533 cm^{-1} , which can also be seen in the spectrum of the Si400m sample (fig. 5.10). It can be seen, that the height of both peaks seems to be related with each other, which indicates that they could be different transitions of the same molecule. The peak at 3737 cm^{-1} is in the typical range of -OH group vibrations. The high energy of the peak at 4533 cm^{-1} suggests, that this peak is a combined

transition of two bonds or a overtone feature. The peaks could not be assigned to any specific molecule.

Both features can also be found in the single beam of an empty cell. This suggests that the features are not related to the nanotubes, which also explains the decrease of the peak after removal of the substrate of SiMax1.

Besides these two peaks, the samples show only the sharp peak 1262 cm^{-1} discussed above and the broad peaks which do not agree with those of other samples or the literature.

The total transmission measured by the signal strength of the interferogram has been observed for the baking process of all samples and is shown in table 5.1. It can be seen that the baking increases the total transmission by 20% to 90%, which can be explained by the removal of impurities from the sample.

T	Si400m	Si400a	SiMax1	SiMax2
RT	2.0 V	-	-	-
150°C	2.4 V	4.1 V	0.16 V	0.80 V
500°C	2.8 V	4.3 V	0.21 V	-
720°C	2.5 V	4.9 V	0.30 V	1.03 V

Table 5.1: The signal strength of the different samples after the different baking temperatures. RT stands for room temperature. The sample Si400m has been removed from the sample holder between the 500°C and the 720°C baking. Because the sample coverage is not uniform a different position of the sample can cause a change in the total transmission. SiMax1 has been baked with a Si substrate and SiMax2 without. The difference in the transmission of both samples indicates an absorption of the Si.

It can be summarized that the spectra of Si samples showed neither agreement with the KBr samples nor with the literature. The higher baking temperatures can reduce the general absorption, which could be used for higher sample amounts. While the infrared measurement of pure SWNTs is apparently complicated and have been published only by one group [3, 28], it is not necessary to detect the nanotubes to conduct measurements on the hydrogen interaction. To allow measurements about the

presence and amount of the nanotubes, they could be especially functionalized to detect the IR-active functionalization groups.

Dropping Method

In order to avoid a possible contamination with filter paper or acetone, a sample has been prepared directly from the nanotube suspension. In the dropping method, which is also used in other spectroscopic observations [3], the Si substrate is heated on a hot plate which is set to 150°C to vaporize the water in the solution. Then 25ml of a 2mg/l solution is dropped on the substrate which equals an amount of 0.05 mg nanotubes. Each drop was given time to vaporize before the next drop was applied. After the dropping the sample showed weak white spots comparable to residua of water stain.

The spectrum of the sample is shown in figure 5.14 and shows vast absorption features, which can be easily assigned to the SDS in the solution. This also explains the white spots visible on the sample.

The sample was baked to 700°C and the pressure of the chamber was observed while heating up. The initial pressure of 10^{-6} torr rose up to 10^{-4} torr at around 400°C and dropped within 1h back to the initial pressure. The spectrum after the baking is also shown in figure 5.14. It can be seen, that the SDS feature is mainly removed, which agrees with increase of pressure at 400°C, but a new feature around 1000-1100 cm^{-1} is present, which can be due to a chemical reaction of the SDS at high temperatures.

Because the SDS and after baking its derivatives are dominating the spectra, no other features are visible. It can be concluded, that the removal of SDS by flushing with DI water is essential for the IR measurements. Due to the high amount of SDS present in this preparation method, the outgassing at 400°C coats the windows even when the steel shield is applied. Therefore the thin film preparation method as described above is preferable, and it shows, that the removal of SDS in the thin film method is effective.

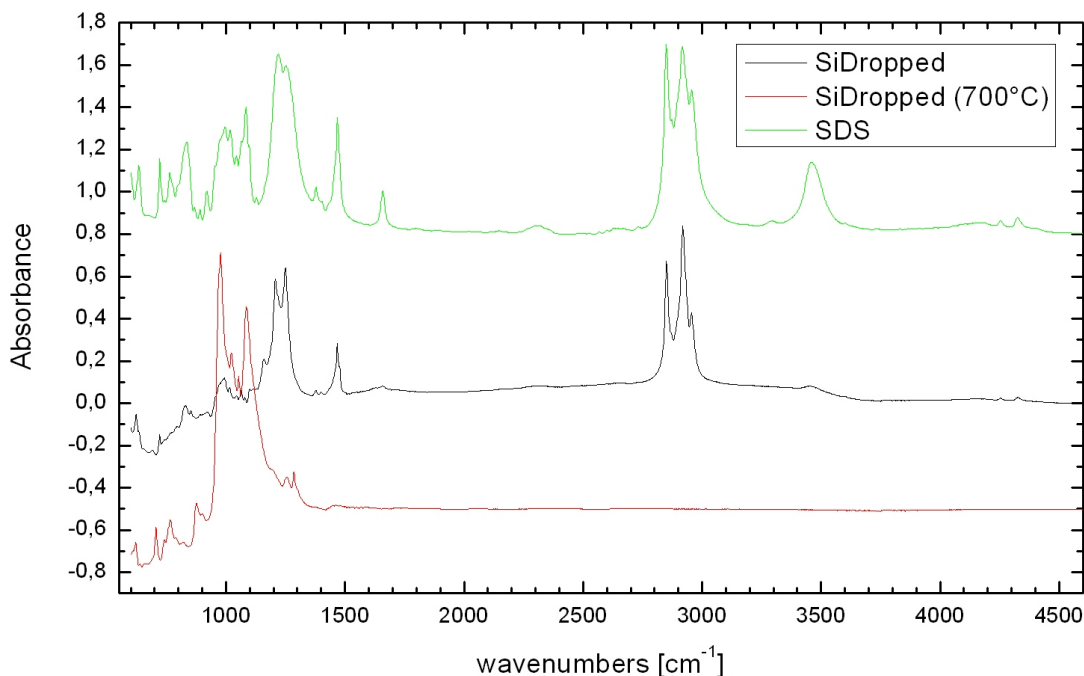


Figure 5.14: Spectrum of the SiDrop sample before and after baking to 700°C. The spectra are taken with the plain Si as a reference, both spectra are at common scale. A spectra of SDS is shown for reference.

To use the dropping method a more concentrated nanotube solution would be necessary to reduce the amount of SDS on the sample. The nanotubes in a more concentrated solution would quickly bundle together to form ropes of nanotubes, which could be avoided by constant sonication during the dropping.

5.3 Hydrogen Measurements

5.3.1 Hydrogen Interactions

As discussed in section 1.3 hydrogen can be stored in carbon nanotubes by physisorption or chemisorption, but physisorption is more probable at our experimental conditions (room temperature, pressure up to 1000 psi). If molecular hydrogen physisorbs on a surface, the electronic distribution of the H_2 molecule is disturbed and therefore it can be detected with infrared measurements. This process is comparable to the pressure induced spectra discussed in section 3.2.

Physisorbed molecules are bound by the van der Waals-force to the surface. This is a relatively weak force, so the distortion of the electronic distribution of the H_2 molecule is small, producing a small dipole moment. Thus the only slightly disturbed hydrogen molecule produces an infrared signal close to the eigenfrequency of the undisturbed molecule at 4246 cm^{-1} . High pressure hydrogen was used to improve the amount of physisorbed molecules and thus to increase the signal.

A high pressure hydrogen spectrum taken at an empty cell is shown in figure 5.15. In agreement with the literature [5] two collision induced bands can be seen. The pure rotational band from 600 cm^{-1} to 1200 cm^{-1} and the rotational vibrational band from 4000 cm^{-1} to 5000 cm^{-1} as described in section 3.2.

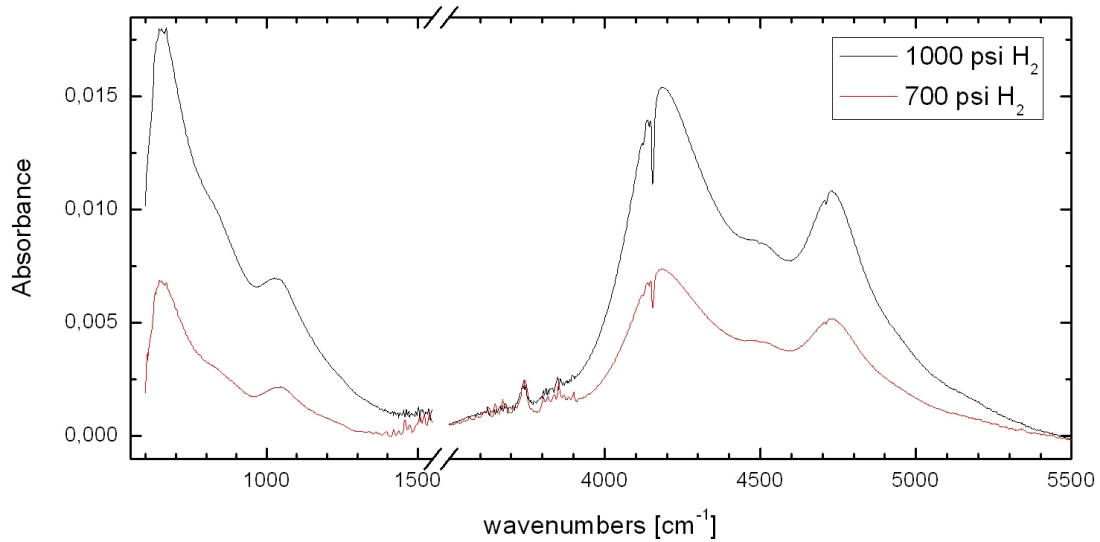


Figure 5.15: Spectra of hydrogen at 700 and 1000 psi. Both spectra are at common scale. Two collision induced bands are in our observational range.

As we can see a possible interaction of hydrogen and nanotubes would be in the range of the high pressure hydrogen spectrum, which would overlay the weak interaction signal. To detect a small signal in this area, we subtract a hydrogen spectrum of an

empty cell from a hydrogen spectrum taken with sample.

$$\ln \left(\frac{\text{sample in vacuum}}{\text{sample in hydrogen}} \right) - \ln \left(\frac{\text{vacuum}}{\text{hydrogen}} \right) \quad (5.1)$$

This show us only the interaction of the hydrogen with the sample material.

The samples have been measured under vacuum, at 700 psi and at 1000 psi, which measures the hydrogen signal *and* a possible interaction feature. Directly before or after these measurements the according hydrogen spectra of the empty cell have been taken to observe only the hydrogen signal. Then both spectra have been subtracted as displayed in figure 5.16 to show the hydrogen interaction with the sample.

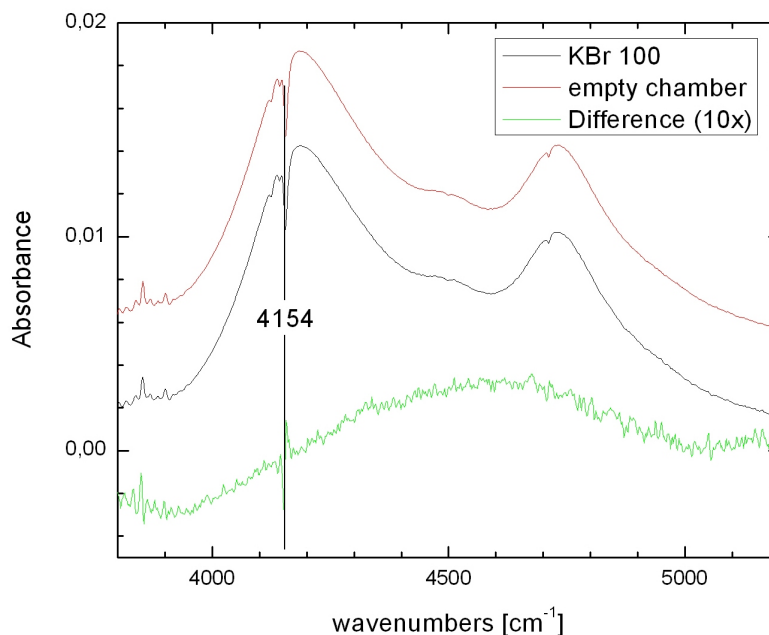


Figure 5.16: Hydrogen spectra of KBr100 and of an empty cell both taken at 1000 psi. The subtraction is ten times magnified for a more detailed view. The subtraction feature at 4154 cm^{-1} is due to the "dip" of the Q-branch.

A typical subtraction spectrum, as it is shown in figure 5.16 shows only one sharp feature at 4154 cm^{-1} . This peak is due to the sharp "dip" in the Q-branch which can be seen in pure hydrogen spectra. As discussed on page 51 a constant sharp feature can easily cause a peak in when taken with reference to itself. Furthermore due to the low reading accuracy of $\pm 25 \text{ psi}$ at the gauge, the hydrogen pressure can vary between

different measurements. Therefore the Q-Branch "dip" changes in height, causing a peak in the subtraction spectra.

To prove that this feature is not related to the sample material, two pure hydrogen spectra from different days have been subtracted from each other. The subtraction also produces this feature and is shown in figure 5.17 for reference.

An overview over the subtraction spectra of all samples is shown in figure 5.17. The feature at 4154 cm^{-1} can be found in all samples.

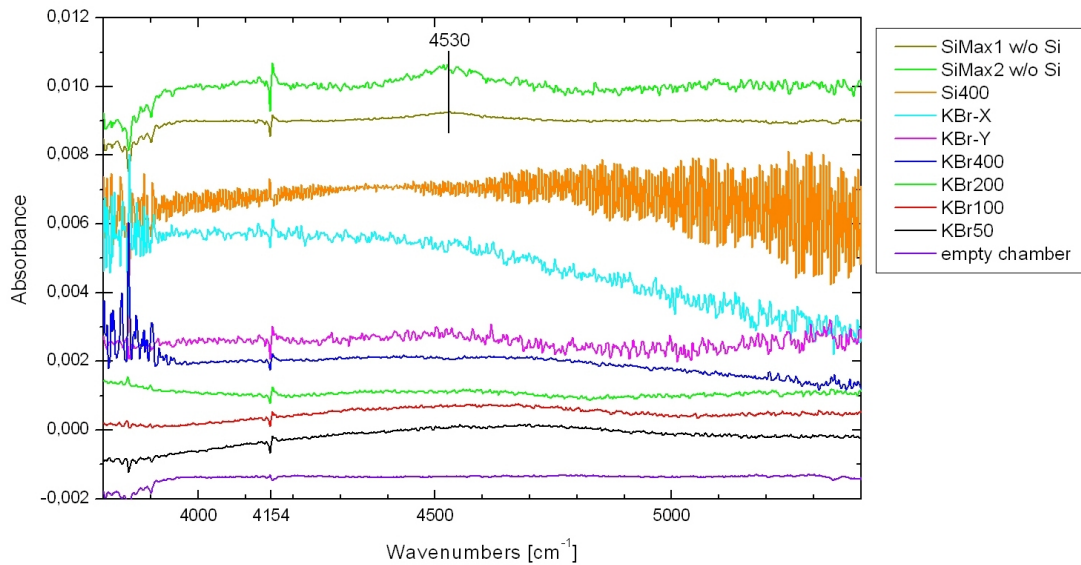


Figure 5.17: Subtraction spectra for the different samples. The spectra have been taken at 1000 psi H_2 with reference to vacuum and are displayed at the same scale. The difference of two pure hydrogen spectra is shown for comparison

The two SiMax samples show a broad feature at 4530 cm^{-1} , which is at the same position as an absorption peak of the sample itself (cf. fig. 5.13). This peak also appears in a difference spectrum which compares the sample without hydrogen at different times. It can be concluded, that the peak is growing over time and thus the peak in the hydrogen spectrum is due to the fact, that the measurements with hydrogen have been taken after the measurements at vacuum. The time evolution of this feature was not studied any further in this work, but can be of interest for further measurements on this system.

Besides these two features, all subtraction spectra are flat, showing no evidence of a hydrogen-nanotube interaction at the given noise level. While the KBr samples of method B show low noise spectra, the samples of method A have a higher noise signal due to a higher general absorbance. The spectrum of Si400 appears to have a high noise level, but instead the signal is disturbed by a wave being an experimental artifact due to interference on parts of the windows. This is a common problem for this cell model and is explained in more detail at [10]. The spectra of the two SiMax samples have been averaged over 10000 cycles to reduce the noise level.

To check for slow adsorption kinetics long time measurements have been conducted for KBr200 (13 hours), Si400 (8 hours) and SiMax1 (12 hours) with similar results.

No hydrogen absorption could be detected which can be explained by two major factors:

1. The infrared signal of the physisorption process is too small. Because the physisorption forces are weak, they induce only a small dipole moment which can not be detected by our measurements. The effect of physisorption on the intramolecular hydrogen bond has been observed with Raman spectroscopy. Williams [19] reported shifts of up to 2 cm^{-1} in the Raman spectra of low pressure hydrogen when physisorbed on SWNTs at cryogenic temperatures, which indicates that the influence of physisorption on the hydrogen molecule is small but in general detectable.
2. There was not enough hydrogen uptake. As discussed in section 1.3 a possible hydrogen uptake at room temperature between 0.15 wt% and 1 wt% can be expected. The hydrogen uptake in our sample could be less due to impure material, not completely opened samples or functional groups blocking the opening ports of the nanotubes. Different chemical treatment could open the nanotubes with a higher yield and high temperature annealing can be used to remove the functional

groups. Additionally the adsorption is affected by geometrical properties of the nanotubes or the nanotube bundles.

An spectroscopic observation of hydrogen uptake has been reported by Mayer [10] working with metal organic frameworks (MOFs) on an identical system, which proves the general adequacy of the used method.

5.3.2 Hydrogen Impurities

As discussed above the exposure to hydrogen showed no interaction feature of physisorbed hydrogen. While special care has been taken in observing the range of the high pressure signal around 4000 cm^{-1} to 5000 cm^{-1} , two other features have been observed in the hydrogen spectrum².

Adsorbed Water

A broad peak centered at 3350 cm^{-1} has been observed in the hydrogen spectra, which can be assigned to adsorbed water. This feature is present on most of the samples, but to a highly varying extend. Figure 5.18 shows this feature on a KBr200 sample at 700 psi and its development in time. As can be seen in figure 5.19 the peak is present in the first measurement, which averages over the first ten minutes of exposure, and is growing continuously over at least 12 hours.

In the usual measurements, which have been taken in the first minutes after filling the chamber this peak can be seen in most of the KBr samples, but can not be seen in the Si-based samples nor in the hydrogen spectra of a plain KBr pellet or an empty cell. The long time measurements of KBr200, Si400 and SiMax all show a grow of this peak, so that it can also be detected on the Si samples after several hours.

²A hydrogen spectrum is a spectrum of hydrogen with reference to a vacuum spectrum, both with the same sample inside.

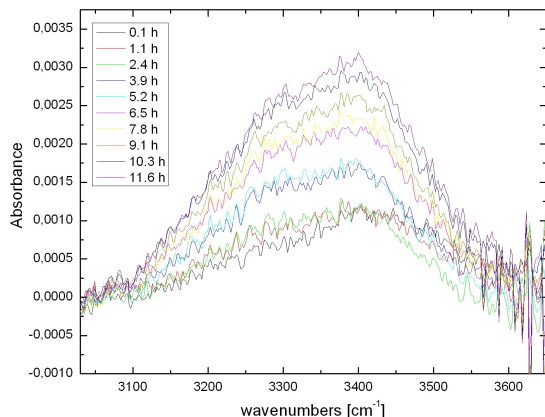


Figure 5.18: The adsorbed water in the hydrogen spectra of KBr200 at 700 psi. The sample was exposed to high pressure over 12 hours. The KBr200 sample shows a strong adsorption feature compared to other samples.

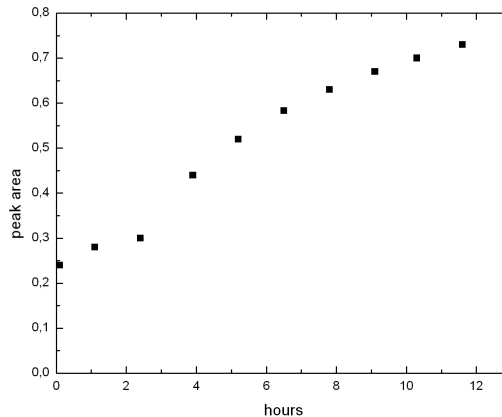


Figure 5.19: The peak area is measured over the exposure time at high pressure. After 12 hours the water feature is still growing, but seems to start saturating.

Even though adsorbed water has been observed on the sample under vacuum (especially if not baked), the fact, that we see this feature in the hydrogen spectra, which has been taken with reference to a vacuum spectra, means that the adsorbed water is related to the introduction of hydrogen.

A similar feature in the hydrogen spectra of metal organic frameworks (MOFs) has been reported by Mayer [10], who worked on the parallel system using the same hydrogen bottle. A measurement with water vapor at room pressure and without hydrogen produced the same peak and confirmed the assignment of adsorbed water [10].

The water is an impurity of the hydrogen as it is reported by the provider [32]. When the cell is filled with hydrogen a certain amount of water is also introduced in the cell and adsorbs on the sample. The more water is adsorbed on the material, the slower additional adsorption takes place, which can be seen in time dependence (fig. 5.19). Water impurities in hydrogen are a known problem in measurements of hydrogen uptake on SWNT [36, 37].

Because the connection to the gas bottle is open during the experiment to maintain a constant pressure, additional water can diffuse from the gas bottle into the cell to increase the adsorption.

The fact, that the amount of adsorbed water depends on the used sample is due to the different hydrophilicity of the samples. Because no adsorbance was detected on a plain KBr pellet, it could be deduced, that the nanotubes, which are a highly porous material adsorb the water. The adsorption feature reported for MOFs using the same system has three times the intensity of the amount observed for SWNTs (both after 12h)[10].

On the other hand the adsorption observed in this work differed for the individual samples but did not scale with amount of nanotubes.

It has to be noted that not all measurements have been done directly after the filling of the cell. Some samples have been exposed to lower pressures before for additional measurements and sometimes the measurement was not taken directly after filling the cell with the designated pressure.

Furthermore the adsorption capability for water introduced by hydrogen depends on the already adsorbed water in the material, as can be deduced from the time evolution discussed above. So the additional uptake due to hydrogen varies with the amount of baking beforehand.

In conclusion the water adsorption by the nanotubes seems more probable than by the substrate. For a more detailed analysis more care has to be taken regarding the baking of the sample and the exposure time before the measurement.

CO₂

The high infrared cross section and the presence in room air makes carbon dioxide inevitable to detect. Even under vacuum conditions a CO₂ signal will always be detected

due to the CO_2 in the spectrometer and therefore the CO_2 in a difference spectra varies randomly due to the changing amount.

Different from those random changes, with the introduction of hydrogen in our cell we see an increase of gaseous carbon dioxide over time as it is shown in figure 5.20.

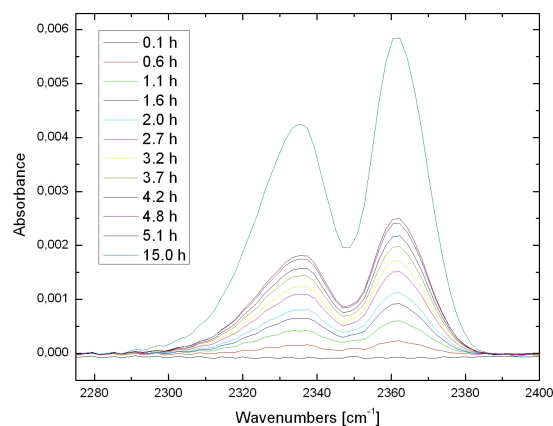


Figure 5.20: The CO_2 grows over time at hydrogen exposure. Spectra taken on a plain KBr pellet at 1000 psi.

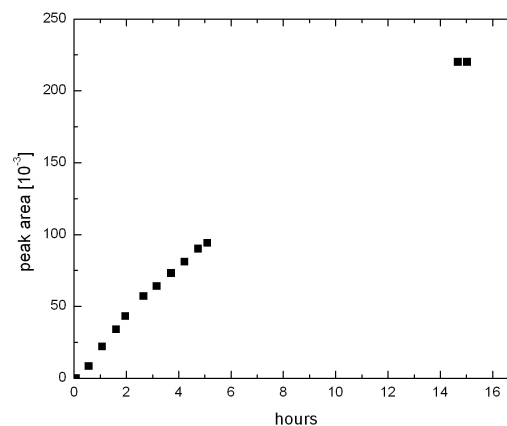


Figure 5.21: Time development of the peak area of the CO_2 peak.

The growth of this feature can be observed in all long time measurement regardless of the sample material or even in an empty chamber. Contrary to the adsorbed water this feature can not be detected immediately after the introduction of the hydrogen. In the here shown spectra of a plain KBr pellet with a very low noise it was detectable after 30 minutes. The difference to water is obvious when comparing the time evolution of both peaks in figure 5.19 and 5.21. Similar results have been found in the parallel system by Mayer [10].

Because the CO_2 is not present in the spectrum directly after filling the chamber, it can not be an impurity of the hydrogen. A possible explanation is, that CO_2 molecules are adsorbed on the walls inside the cell and can not be completely removed by the baking process. When the hydrogen at high pressure is induced into the cell, the hydrogen molecules are hitting the walls at high kinetic energy and releasing the adsorbed CO_2 , similar to the sputtering process used in surface physics.

Chapter 6

Summary

The physisorption of hydrogen on Single Walled Carbon Nanotubes (SWNTs) has been spectroscopically studied by transmission fourier transform infrared spectroscopy at pressures up to 1000 psi and at ambient temperature.

A sample preparation technique has been developed to apply thin films of SWNTs to KBr or Si substrates, which reduces the amount of contaminations compared to other techniques explored. Samples with different amounts of carbon nanotubes have been prepared, which showed a broad general absorption scaling with the applied amount, but did not show spectral evidence of the SWNTs or of functional groups attached to them. The broad general absorption limits the maximum amount of nanotubes on a sample, which can still be observed in transmission

It has been shown, that the broad absorption is due to scattering on the SWNT bundles, which can be reduced by up to 50% by applying a refractive index matching liquid. Furthermore baking up to 700°C can increase the transmission by up to 90%, which allows the observation of higher sample amounts.

The measurements at high pressure showed no collision induced features of the intrinsically IR-inactive hydrogen molecules. This shows that the hydrogen dipole moment, produced by the shift in the electronic distribution of the H₂ molecule due to the physisorption on SWNTs, lies below the sensitivity of the spectrometer for samples of up to 2.1 mg of nanotubes.

At the introduction of hydrogen, water as an impurity of the hydrogen has been observed, which adsorbed on the sample surface. Also an increase in the gaseous CO_2 has been detected, which can be caused by adsorbed CO_2 on the cell wall which is sputtered off by the impact of the hydrogen molecules at high pressure.

Appendix A

Reference Spectra

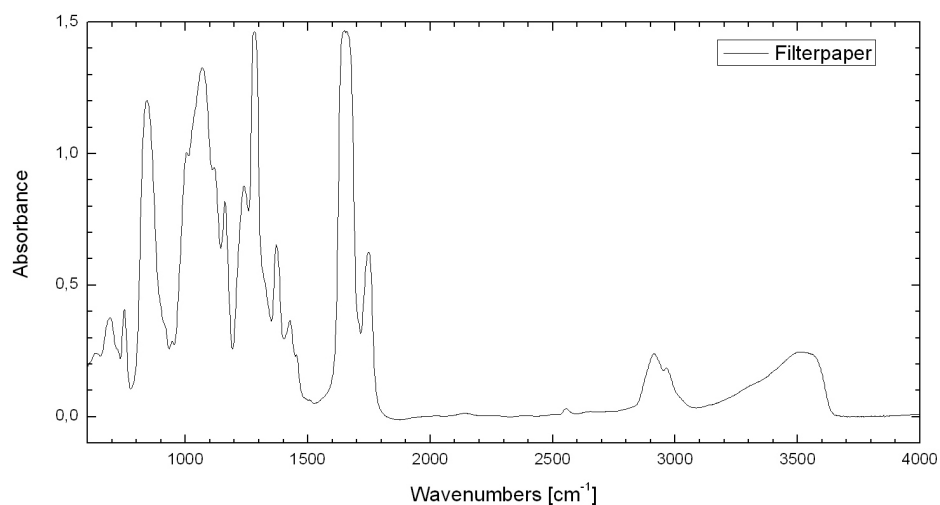


Figure A.1: A filter paper was dissolved in an acetone bath. A KBr pellet was first submerged in the solution and then dried in vacuum, evaporating the acetone with only filter paper remaining. The amount of filter paper was about ten times higher than what a sample is exposed to before it is flushed with fresh acetone.

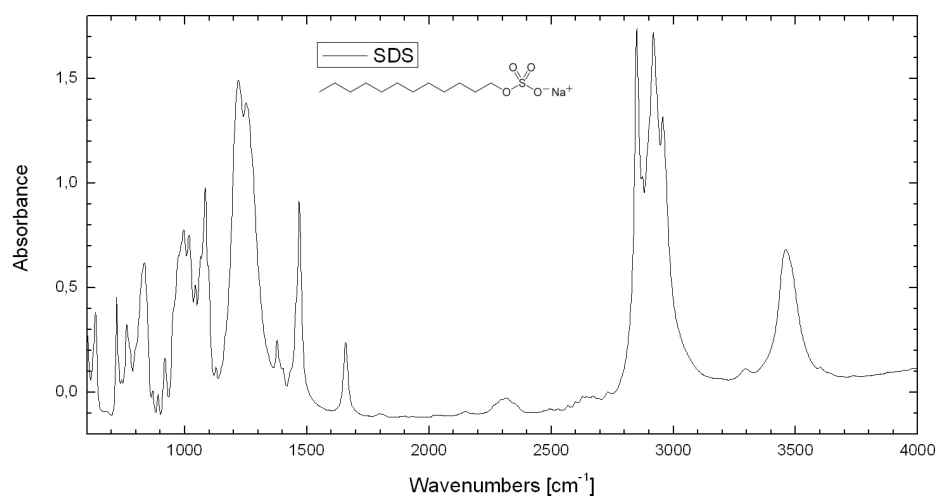


Figure A.2: 16 mg of SDS (sodium dodecyl sulfate) have been pressed on top of a usual 200mg KBr pellet.

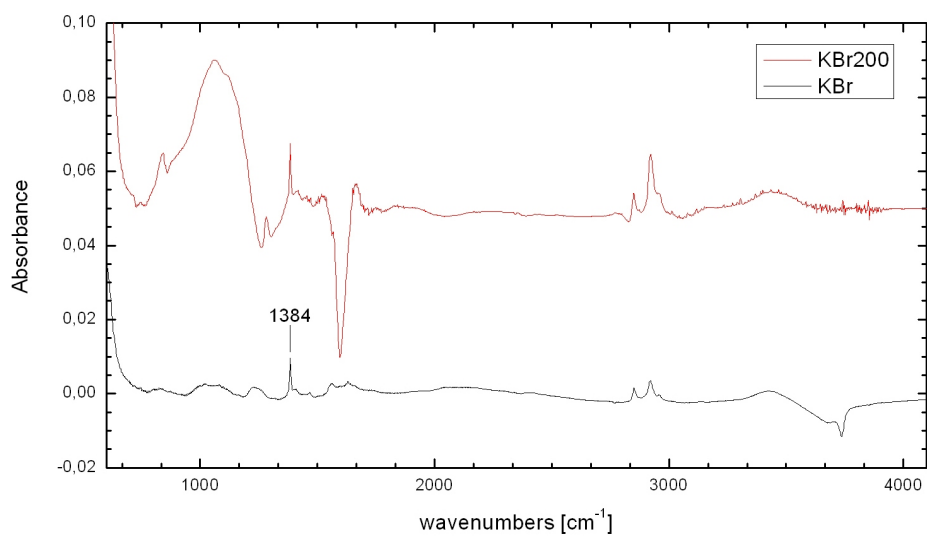


Figure A.3: The spectrum of a plain KBr pellet and of the KBr200 sample for comparison. Both spectra are at the same scale but are vertically shifted for better display.

Appendix B

Cleaning of Silicon

The cleaning process of silicon consists of the following steps:

1. Rinse it in acetone, methanol and finally water (the water is necessary, because hydrogen peroxide is reactive with some organic solvents).
2. Put it for 10min at 80°C in a 4:1:1 solution of water, hydrogen peroxide and ammonium hydroxide.
3. Rinse it with water.
4. Put it for 10min at 80°C in a 4:1:1 solution of water, hydrogen peroxide and hydrochloric acid.
5. Rinse it with water and remove the water with a stream of nitrogen gas.

Step 2 and 4 of this process are known as *Standard Clean 1* (SC1) and *Standard Clean 2* (SC2) and are a standard procedure to clean silicon. SC1 oxidizes organic contaminations while SC2 removes metal particles [38].

This process produces a clean silicon sample, which is passivated by a native oxide layer on the surface.

References

- [1] S. Satyapal. DOE hydrogen program 2006 progress report. page 273, 2006.
- [2] E. Unulan. *Single walled carbon nanotube thin films: properties and applications*. PhD thesis, Rutgers University, 2006.
- [3] U. Kim. Infrared-active vibrational modes of single-walled carbon nanotubes. *Physical Review Letters*, 95, 2005.
- [4] H. Haken. *Molecular Physics and Elements of Quantum Chemistry*. Springer, 2004.
- [5] H. L. Welsh. Pressure induced absorption spectra of hydrogen. *Int. Review of Science Physical Chemistry*, page 33, 1972.
- [6] A. Chambers. *Basic Vacuum Technology, 2nd Ed.* Institue of Physics Publishing, 1998.
- [7] L. Schlapbach. Hydrogen-storage materials for mobile applications. *Nature*, 414:353, 2001.
- [8] R.v. Helmolt. Fuel cell vehicles: Status 2007. *Journal of power sources*, 165:833, 2007.
- [9] S. Satyapal. The U.S. department of energy national hydrogen storage project: Progress towards meeting hydrogen-powered vehicle requirements. *Catalysis Today*, 120:246, 2007.
- [10] D. Mayer. A fourier transform - infrared spectroscopy study of hydrogen interaction with metal-organic-frameworks. Master's thesis, Rutgers University, 2007.
- [11] A. Dillon. Storage of hydrogen in single-walled carbon nanotubes. *Nature*, 386:377, 1997.
- [12] C. Liu. Hydrogen storage in single-walled carbon nanotubes at room temperature. *Science*, 286:5442, 1999.
- [13] Y. Ye. Hydrogen adsorption and cohesive energy of single-walled carbon nanotubes. *Applied Physics Letters*, 74(16):2307, 1999.
- [14] G. Tibbets. Hydrogen storage capacity of carbon nanotubes, filaments, and vapor-grown fibers. *Carbon*, 39:2291, 2001.
- [15] A. Dillon. Hydrogen storage in carbon-based materials. *DOE Hydrogen Program: Progress Report*, 2004.

- [16] P. Bernard. Storage of hydrogen by physisorption on carbon and nanostructured materials. *Scripta Materialia*, 56:803, 2007.
- [17] R. Zacharia. Intrinsic linear scaling of hydrogen storage capacity of carbon nanotubes with the specific surface area. *Catalysis Today*, 120:426, 2007.
- [18] M. Becher. Hydrogen storage in carbon nanotubes. *C.R. Physique*, 4:1055, 2003.
- [19] K. Williams. Raman spectroscopic investigation of H₂, HD, and D₂ physisorption on ropes of single-walled carbon nanotubes. *Phys. Rev. Lett.*, 88(16):165502, Apr 2002.
- [20] A. Centrone. Adsorption of H₂ on carbon-based materials: A raman spectroscopy study. *Physical Review B*, 71:245406, 2005.
- [21] I. Bashkin. Thermally stable hydrogen compounds obtained under high pressure on the basis of carbon nanotubes and nanofibers. *JETP LETTERS*, 79:226, 2004.
- [22] F. Darkrim. Review of hydrogen storage by adsorption in carbon nanotubes. *International Journal of Hydrogen Energy*, 27:193, 2002.
- [23] S Iijima. Helical microtubules of graphitic carbon. *Nature*, 354:56, 1991.
- [24] P. Nikolaev. Gas-phase catalytic growth of single-walled carbon nanotubes from carbon monoxide. *Chemical Physics Letters*, 313:1999, 1999.
- [25] S. Tsang. A simple chemical method of opening and filling carbon nanotubes. *Nature*, 372:159, 1994.
- [26] A. Kuznetsova. Enhancement of adsorption inside of single-walled nanotubes: opening the entry ports. *Chemical Physics Letters*, 321:292, 2000.
- [27] M.S. Dresselhaus. *Science of Fullerenes and Carbon Nanotubes*. Academic Press, 1996.
- [28] U. Kim. Raman and IR spectroscopy of chemically processed single walled carbon nanotubes. *Journal of the American Chemical Society*, 127:15437, 2005.
- [29] R. Shankar. *Principles of Quantum Mechanics 2nd Edition*. Springer, 1994.
- [30] H. L. Welsh. The pressure induced infrared spectrum of hydrogen and its application to the study of planetary atmospheres. *Journal of the Atmospheric Sciences*, 26:835, 1969.
- [31] J. Van Kranendonk. Intercollisional interference effects in pressure-induced infrared spectra. *Canadian Journal of Physics*, 46:1173, 1968.
- [32] Test result for individual gas lot. *phone call with Gas Technology Service (GTS) on 06/27/07*.
- [33] User manual for the high temperature high pressure cell, Specac.
- [34] National Institute of Standards and Technology. NIST chemistry webbook. <http://webbook.nist.gov/>.

- [35] G. Herzberg. *Spectra of Diatomic molecules*. Van Nostrand, 1950.
- [36] R. Yang. Hydrogen storage by alkali-doped carbon nanotubes-revisited. *Carbon*, 38:623, 2000.
- [37] R. Yang. *Adsorbents: Fundamentals and Applications*. John Wiley, 2003.
- [38] Werner Kern. *Handbook of Semiconductor Wafer Cleaning Technology*. Noyes Publications, 1993.